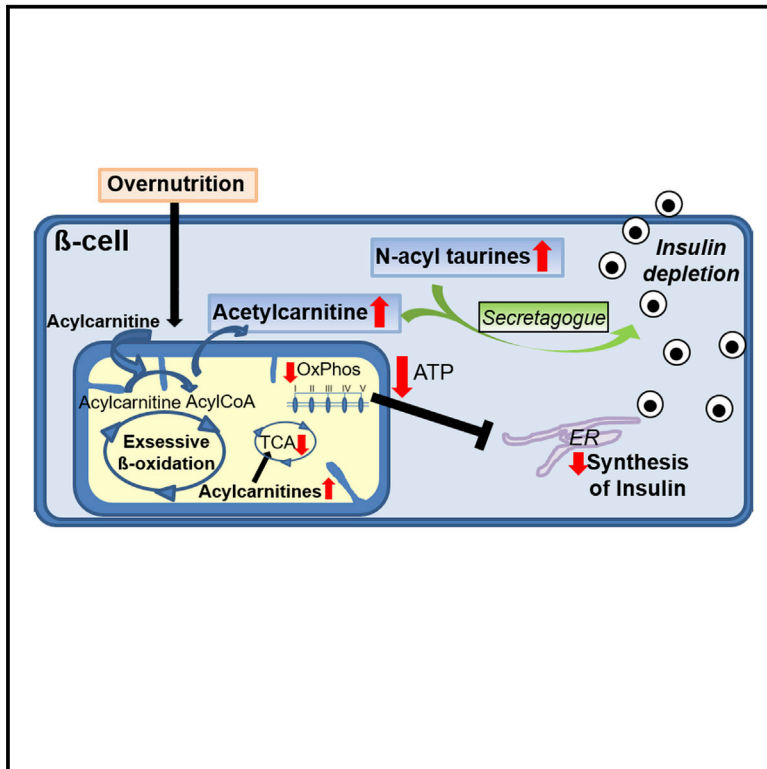


# N-acyl Taurines and Acylcarnitines Cause an Imbalance in Insulin Synthesis and Secretion Provoking $\beta$ Cell Dysfunction in Type 2 Diabetes

## Graphical Abstract



## Authors

**Michaela Aichler, Daniela Borgmann,  
Jan Krumsiek, ..., Susanne Neschen,  
Matthias H. Tschöp, Axel Walch**

## Correspondence

michaela.aichler@  
helmholtz-muenchen.de (M.A.),  
axel.walch@  
helmholtz-muenchen.de (A.W.)

## In Brief

Aichler et al. used a MALDI mass spectrometry-based systems approach to characterize molecular interaction networks of functional pathways in mouse and human pancreatic tissues. They identify classes of metabolites involved in insulin synthesis and secretion, which are disrupted in diabetes.

## Highlights

- Investigation of  $\beta$  cells' pathophysiology directly in T2D pancreatic tissue
- $\beta$  cell dysfunction results from arrest of insulin synthesis and enhanced secretion
- Insulin synthesis arrest is caused by accumulation of stearyl carnitine
- Insulin secretion is caused by accumulation of N-acyl taurines and acetyl carnitine

# N-acyl Taurines and Acylcarnitines Cause an Imbalance in Insulin Synthesis and Secretion Provoking $\beta$ Cell Dysfunction in Type 2 Diabetes

Michaela Aichler,<sup>1,\*</sup> Daniela Borgmann,<sup>1</sup> Jan Krumsiek,<sup>2,3</sup> Achim Buck,<sup>1</sup> Patrick E. MacDonald,<sup>4,5</sup> Jocelyn E. Manning Fox,<sup>4,5</sup> James Lyon,<sup>4</sup> Peter E. Light,<sup>4,5</sup> Susanne Keipert,<sup>3,6</sup> Martin Jastroch,<sup>3,6</sup> Annette Feuchtinger,<sup>1</sup> Nikola S. Mueller,<sup>2</sup> Na Sun,<sup>1</sup> Andrew Palmer,<sup>7</sup> Theodore Alexandrov,<sup>7,8,9</sup> Martin Hrabe de Angelis,<sup>3,10,12</sup> Susanne Neschen,<sup>3,10</sup> Matthias H. Tschöp,<sup>3,6,11</sup> and Axel Walch<sup>1,13,\*</sup>

<sup>1</sup>Research Unit Analytical Pathology

<sup>2</sup>Institute of Computational Biology

Helmholtz Zentrum München, Neuherberg 85764, Germany

<sup>3</sup>German Center for Diabetes Research (DZD), Ingolstädter Landstr. 1, Neuherberg 85764, Germany

<sup>4</sup>Alberta Diabetes Institute

<sup>5</sup>Department of Pharmacology

University of Alberta, Edmonton T6G 2E1, Canada

<sup>6</sup>Institute for Diabetes and Obesity, Helmholtz Zentrum München, Neuherberg 85764, Germany

<sup>7</sup>Structural and Computational Biology Unit, European Molecular Biology Laboratory (EMBL), Heidelberg 69117, Germany

<sup>8</sup>Skaggs School of Pharmacy and Pharmaceutical Sciences, University of California San Diego, La Jolla, CA 92093, USA

<sup>9</sup>SCiLS GmbH, 28359 Bremen, Germany

<sup>10</sup>Institute of Experimental Genetics, Helmholtz Zentrum München, German Research Center for Environmental Health, Ingolstädter Landstrasse 1, Neuherberg 85764, Germany

<sup>11</sup>Division of Metabolic Diseases, Department of Medicine, Technische Universität München, 80333 Munich, Germany

<sup>12</sup>Chair of Experimental Genetics, School of Life Science Weihenstephan, Technische Universität München, Alte Akademie 8, 85354 Freising, Germany

<sup>13</sup>Lead Contact

\*Correspondence: [michaela.aichler@helmholtz-muenchen.de](mailto:michaela.aichler@helmholtz-muenchen.de) (M.A.), [axel.walch@helmholtz-muenchen.de](mailto:axel.walch@helmholtz-muenchen.de) (A.W.)

<http://dx.doi.org/10.1016/j.cmet.2017.04.012>

## SUMMARY

The processes contributing to  $\beta$  cell dysfunction in type 2 diabetes (T2D) are uncertain, largely because it is difficult to access  $\beta$  cells in their intact immediate environment. We examined the pathophysiology of  $\beta$  cells under T2D progression directly in pancreatic tissues. We used MALDI imaging of Langerhans islets (LHIs) within mouse tissues or from human tissues to generate in situ-omics data, which we supported with in vitro experiments. Molecular interaction networks provided information on functional pathways and molecules. We found that stearyl carnitine accumulated in  $\beta$  cells, leading to arrest of insulin synthesis and energy deficiency via excessive  $\beta$ -oxidation and depletion of TCA cycle and oxidative phosphorylation metabolites. Acetylcarnitine and an accumulation of N-acyl taurines, a group not previously detected in  $\beta$  cells, provoked insulin secretion. Thus,  $\beta$  cell dysfunction results from enhanced insulin secretion combined with an arrest of insulin synthesis.

## INTRODUCTION

Despite substantial research efforts, the processes underlying  $\beta$  cell dysfunction in type 2 diabetes (T2D) remain uncertain,

mainly because  $\beta$  cells are technically difficult to access (Marciniak et al., 2014; Poitout and Robertson, 2008; Prentki et al., 2013). For many years, the best approach was to study insulin-secreting  $\beta$  cells, cell lines, or dispersed primary cells; however, the culture conditions for those systems can strongly affect experimental results (Marciniak et al., 2014; Poitout and Robertson, 2008; Prentki et al., 2013). Isolated Langerhans islets (LHIs) are another widely accepted model system, but LHIs can be damaged during isolation and purification (Morini et al., 2006), which involve substantial chemical and mechanical distress inducing considerable changes in cell physiology (Ahn et al., 2007; do Amaral et al., 2013; Irving-Rodgers et al., 2014; Negi et al., 2012). Therefore, explorations of LHI physiology and pathophysiology in model systems may not represent the situation in vivo (Marciniak et al., 2014; Prentki et al., 2013). There is a clear demand for investigations of the pathophysiology of  $\beta$  cells in their intact, immediate environment to allow more meaningful conclusions about their potential function in vivo (Marciniak et al., 2014).

Recent progress in matrix-assisted laser desorption/ionization mass spectrometry imaging (MALDI-MSI) has enabled the direct analysis of the distribution of various analytes in tissues without the need for analyte purification or further manipulation steps (Aichler and Walch, 2015; Norris and Caprioli, 2013). MALDI-MSI enables the creation of in situ-omics data directly from histological tissue sections (Aichler and Walch, 2015; Norris and Caprioli, 2013). Through a combination of molecular mass spectrometric, microscopic, and histological analyses, MALDI-MSI allows specific and sensitive molecular analyses

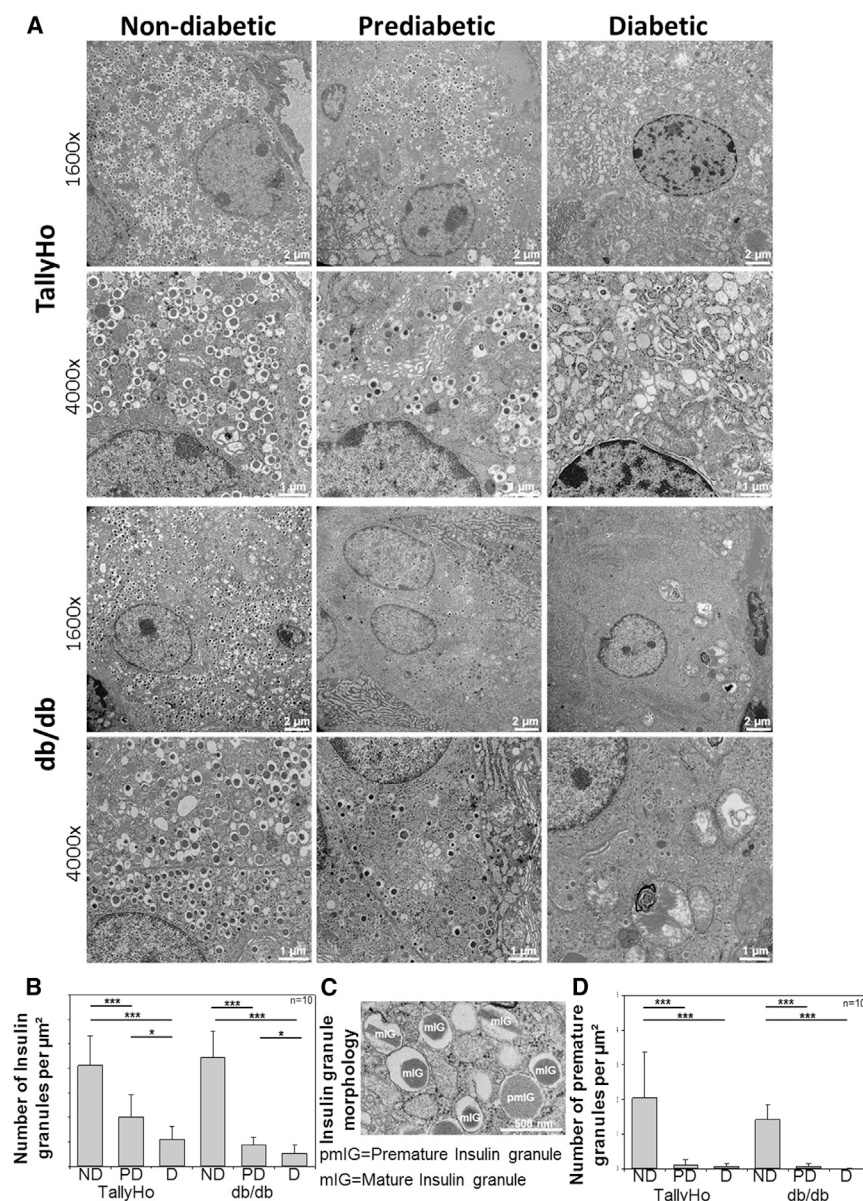


**Figure 1. Early Onset of Insulin Granule Reduction in  $\beta$  Cells**

(A) Electron micrographs from TallyHo and db/db mice. Reduction of insulin granules was evident in PD mice and markedly progressed in D mice. Alterations in endoplasmic reticulum (TallyHo) and mitochondria (TallyHo and db/db) could be seen. (B) Quantification of total numbers of insulin granules.

(C) Insulin granule morphology.

(D) The number of premature insulin granules was reduced in PD and D mice. All data are presented as mean  $\pm$  SEM (ND, non-diabetic; PD, prediabetic; D, diabetic).

## RESULTS

### Changes in Cell Metabolism Are Strongly Related to T2D Progression

We used two mouse models to identify genetic background-independent metabolic alterations of  $\beta$  cells in T2D. BKS.Cg-Cock7m+/+Leprdb/J (db/db) mice (Konstantopoulos et al., 2012; Liang et al., 2012) are widely used for diabetes drug testing; however, they develop monogenic obesity due to disrupted leptin receptor signaling. In contrast, TallyHo/JngJ (TallyHo) mice recapitulate broader aspects of polygenic human “diabetes” (Kim et al., 2001). Based on their phenotypic parameters, we used PD and D animals as well as non-diabetic controls (Figure S1; Table S1A). In total, 263 LHIs in mice were analyzed for in situ metabolomics, in situ proteomics, and hormone content (Table S1). We used histopathological, immunofluorescence, and quantitative image analyses to determine the overall quality and composition of mouse LHIs and MALDI-MSI to determine the hormonal content (Figures S2 and S3A).

of LHIs directly within the exocrine pancreas in unprecedented detail.

To elucidate the mechanisms of  $\beta$  cell dysfunction in T2D, we investigated the molecular pathophysiology of LHIs obtained from prediabetic (PD) and overtly diabetic (D) mice. We used in situ-omics data to investigate metabolic, proteomic, and hormonal alterations in 265 well-characterized mouse LHIs. Using a systems biological approach, we generated molecular interaction networks of functional pathways and molecular classes to build a global map of the molecules associated with  $\beta$  cell dysfunction. We integrated changes in newly discovered molecular classes and developed a mechanistic model of  $\beta$  cell dysfunction. We demonstrated, in LHIs isolated from humans with T2D, the translational relevance of our results and performed in vitro experiments to confirm the causal roles of the observed molecular changes and the effects on  $\beta$  cells in T2D.

Especially under prediabetic conditions, the cellular composition in our mouse models was comparable to those in controls. The hormone contents were altered, as it is also demonstrated by quantification of insulin granules by electron microscopy (Figure 1). We used isolated LHIs ( $n = 54$ ) from healthy humans and patients with T2D and measured their hormonal composition by MALDI-MSI, too (Figure S3B). Both mouse and human LHIs had decreased insulin content under diseased conditions (Figures S3A and S3B). Electron microscopic analysis of  $\beta$  cells from PD mice revealed a significant reduction of insulin granules, which was exacerbated in  $\beta$  cells from D mice (Figures 1A and 1B). The number of premature insulin granules was strongly reduced in  $\beta$  cells from PD and D mice, indicating an early onset of insulin production arrest (Figures 1C and 1D).

To determine the metabolic characteristics of LHIs during T2D progression, we measured the abundance of metabolites in LHIs

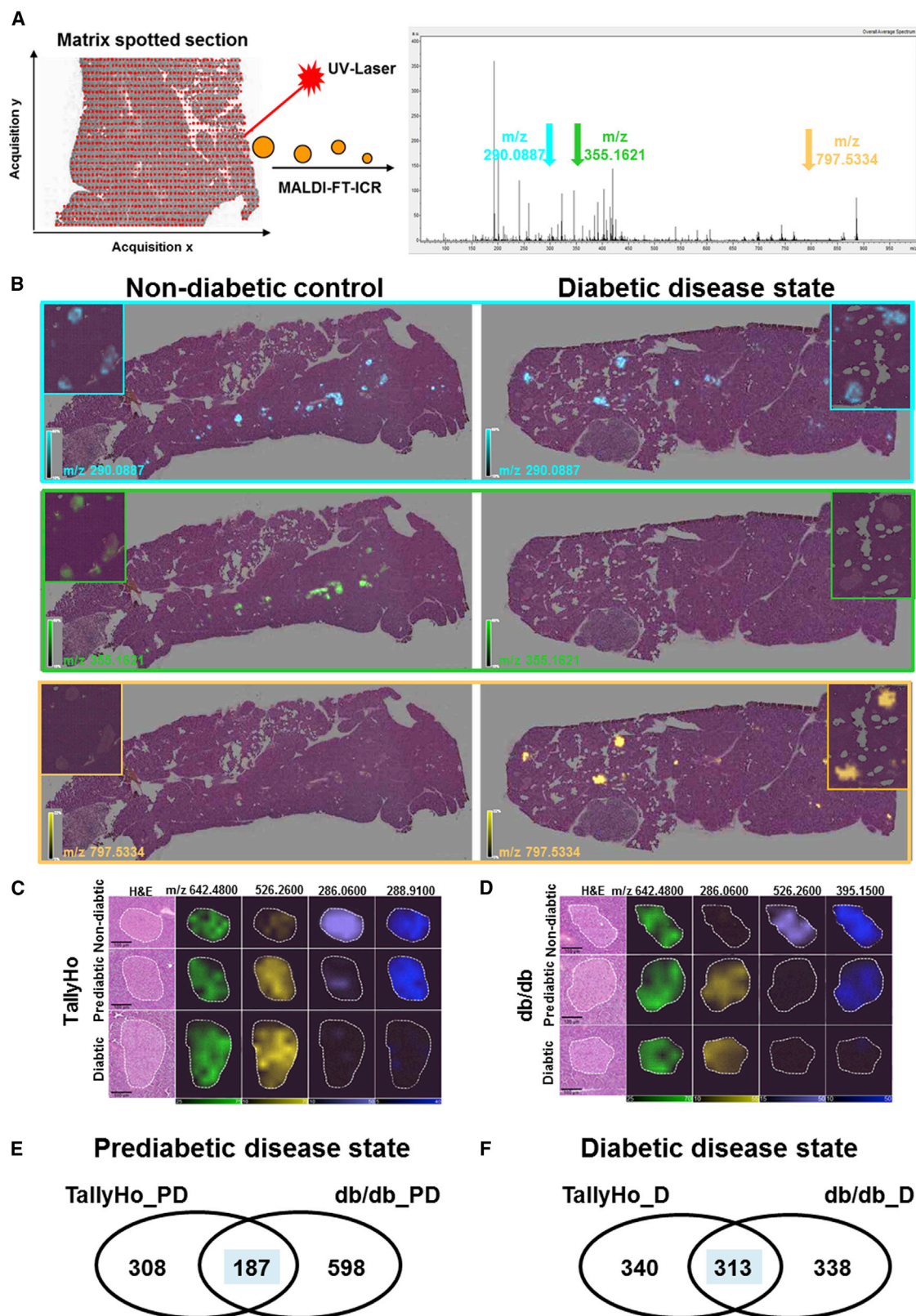


**Figure 2. MALDI Imaging Mass Spectrometry of Langerhans Islets**

(A) A pancreatic tissue section was coated with matrix, which extracts molecules from the tissue. Afterward, the sample was measured in a raster process in the mass spectrometer, resulting in spatially resolved mass spectra.

(legend continued on next page)

directly in mouse pancreatic tissue sections by MALDI-MSI (Figures 2A and 2B). We excluded areas of the exocrine pancreas from all analyses by defining regions of interests around the LHIs and extracting mass spectrometric profiles exclusively from the LHIs (Figures 2C and 2D). The resulting in situ metabolomics data demonstrated a clear molecular separation between the PD and D mice (Figure S4). By comparing the metabolite patterns with those of the respective non-diabetic controls, we determined characteristic abundances of specific disease-related metabolites (Figures 2C and 2D). We identified 495 and 653 metabolites in TallyHo PD and D mice, respectively, and 785 and 651 metabolites in db/db PD and D mice, respectively, that separated the diseased mice from the non-diabetic controls (Table S1B).

To determine which metabolic alterations were independent of the genetic background, we identified the subset of altered metabolites that were common to both mouse models. Within each specific disease state, 187 “PD metabolites” were common to TallyHo and db/db PD mice (Figure 2E), and 313 “D metabolites” were common to TallyHo and db/db D mice (Figure 2F). We defined those two datasets as being representative alterations in PD and D mice, respectively.

Blood glucose concentration is generally used to discriminate between PD and D disease states. Blood glucose levels correlated significantly with 49.2% of the PD and 21.4% of the D metabolites (Tables S2A and S2B). Furthermore, 61.5% of the PD and 15.0% of the D metabolites were directly correlated with the insulin content of the respective LHIs (Tables S3A and S3B).

### Metabolic Pathways in T2D Progression

We made a global map of the metabolites associated with  $\beta$  cell dysfunction and T2D progression (Figure 3; Figure S5). We used Gaussian graphical models to infer statistical links among the metabolites. That method was previously used to reconstruct true metabolic pathways in a statistical fashion (Krumstiek et al., 2011, 2012; Shin et al., 2014). We further analyzed the metabolites that formed the largest cluster (the PD and D “core networks”) and annotated them. Using the metabolites in the core networks that had available KEGG (<http://www.kegg.jp>) annotation, we performed metabolic pathway analyses and identified the pathway networks that characterized  $\beta$  cell degeneration in each disease state (Figures 3A and 3B). We plotted the abundances of the metabolites in the identified pathway networks against the insulin content of the LHIs (Table S3). Metabolites involved in purine, pyrimidine, amino sugar, and nucleotide sugar metabolism were significantly correlated with the insulin content (Figures 4A–4C). In purine metabolism, the diseased LHIs contained less adenosine derivatives and guanosine monophosphate (GMP) and inosine monophosphate (IMP) than the control LHIs (Figure 4D). In pyrimidine metabolism, the diseased LHIs contained less thymidine derivatives and more uridine diphosphate (UDP)-related metabolites than the control LHIs (Figure 4E) and cytidine, which had the most correlations with

other molecules (Figure 3A, indicated in blue), suggesting a central role of this metabolite. In amino sugar and nucleotide sugar metabolism, all of the annotated metabolites were highly abundant in the diseased LHIs, relative to those in controls (Figure 4F). Metabolites related to the biosynthesis of amino acids were generally less abundant in the mouse LHIs than in human LHIs compared to controls (Figure 4G). In the human LHIs, metabolites related to the pentose phosphate pathway and unsaturated fatty acid (FA) biosynthesis were highly abundant relative to those in controls (Figures 4H and 4I).

### Acylcarnitine Accumulation Suppresses Energy Production for Insulin Synthesis but Acetylcarnitine Enhances Insulin Secretion

In the metabolic networks, especially in the PD core network, acylcarnitines had multiple correlations to other molecules and metabolic pathways, suggesting a strong involvement in T2D progression (Figure 3A, brown circle). Acylcarnitines are important intermediates in the FA metabolism, an important energy source for  $\beta$  cells (McGarry, 2002; Prentki et al., 2013; Saponaro et al., 2015). We found that stearyl-, palmitoyl-, linoleoyl-, and acetylcarnitine were more abundant in the LHIs of diseased mice than in those of non-diabetic controls (Figure 5A). Stearoylcarnitine was negatively correlated with insulin content ( $R = -0.386$ ;  $p \leq 0.01$ ; Figure 5B), suggesting that its accumulation might negatively influence insulin content. In contrast, acetylcarnitine was positively correlated with insulin content ( $R = 0.66$ ;  $p \leq 0.001$ ; Figure 5B). Stearyl-, palmitoyl-, and acetylcarnitine were more abundant in LHIs from humans with T2D than in healthy donors, too (Figure 5C).

Acylcarnitine accumulation might result from defective CPT1 and CPT2 shuttling, which is needed to transform FAs into acylcarnitines for entry into the mitochondria (McGarry, 2002; Prentki et al., 2013; Saponaro et al., 2015). We analyzed the expression of CPT1 and CPT2 by immunohistochemistry (Figure S6) and found no significant difference among non-diabetic, PD, and D mice. Therefore, we excluded the CPT1 and CPT2 shuttle system as a reason for the acylcarnitine accumulation.

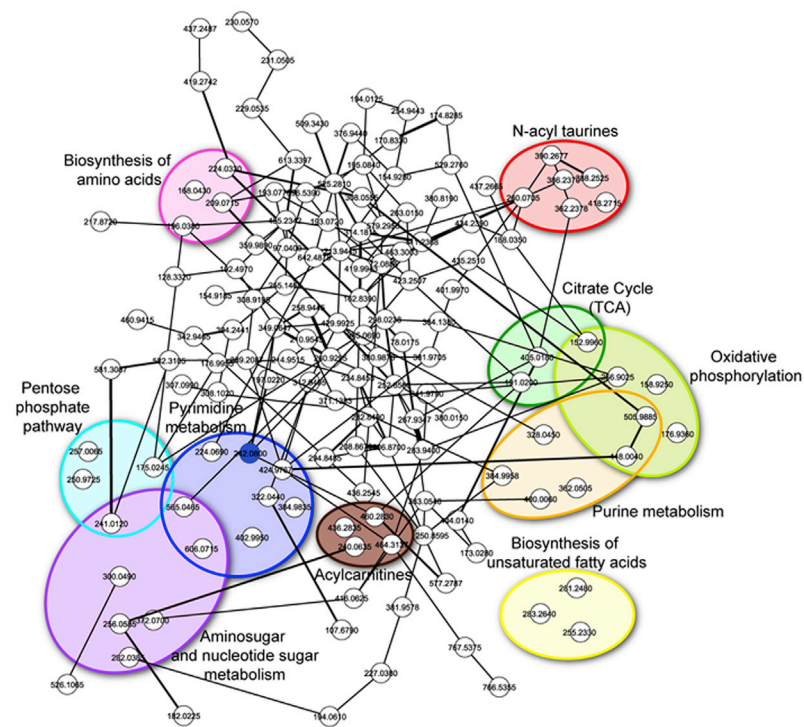
We performed in vitro experiments to determine the functional roles of acylcarnitine accumulation in  $\beta$  cell dysfunction. Under high-glucose conditions,  $\beta$  cells (Min6) treated with acetylcarnitine increased insulin secretion ( $p \leq 0.001$ ), whereas treatment with stearoylcarnitine did not influence insulin secretion (Figure 5D), supporting our observations that acetylcarnitine accumulation correlated with increased insulin secretion (Figure 5B). We counted insulin granules (premature and mature) in similarly treated cells using electron microscopy (Figures 5E–5H). Relative to that in control cells, the total number of insulin granules was comparable in acetylcarnitine-treated cells but reduced in stearoylcarnitine-treated cells (Figures 5E, 5G, and 5H). Similarly, the number of premature insulin granules was reduced in the stearoylcarnitine-treated cells ( $p \leq 0.001$ ), but not in the acetylcarnitine-treated cells (Figures 5F–5H). We concluded that

(B) The UV laser only hits the matrix crystals and does not affect the tissue section, which could be stained after the measurement and used for morphology-directed extraction of mass spectrometric profiles. Examples of visualizations of three different molecules are depicted.

(C and D) Mass spectrometric profiles for the disease stages specific for TallyHo (C) and db/db (D) were generated.

(E and F) Venn diagram of the number of metabolites for the mouse models in prediabetic (E) and diabetic (F) states.

## A Prediabetic core network



## B Diabetic core network

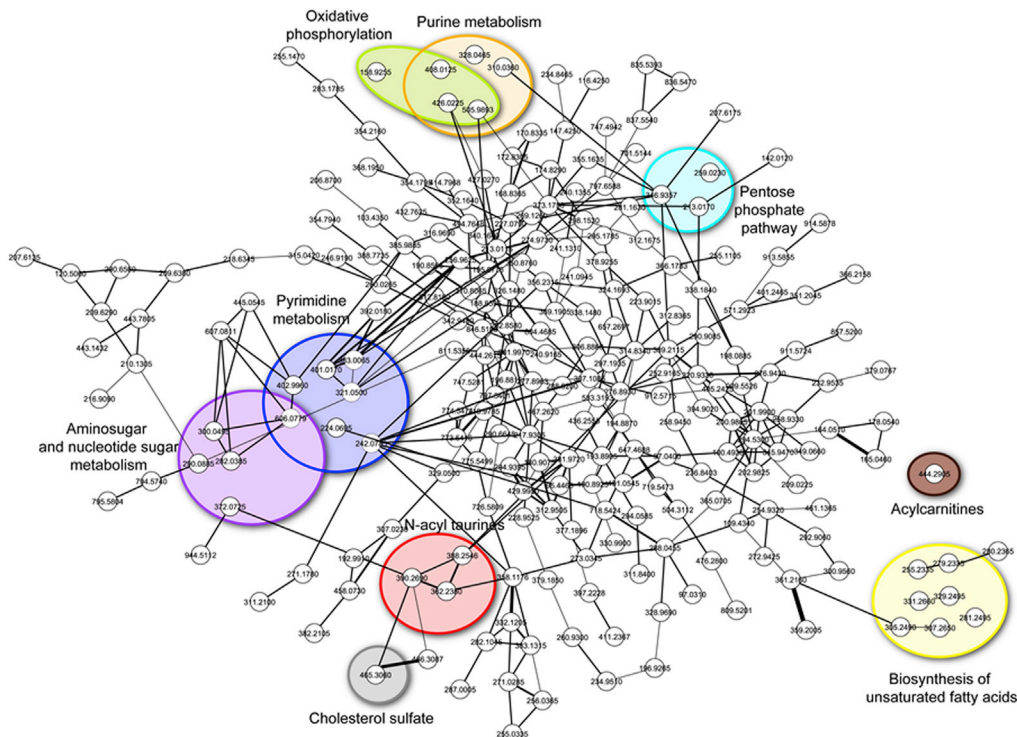
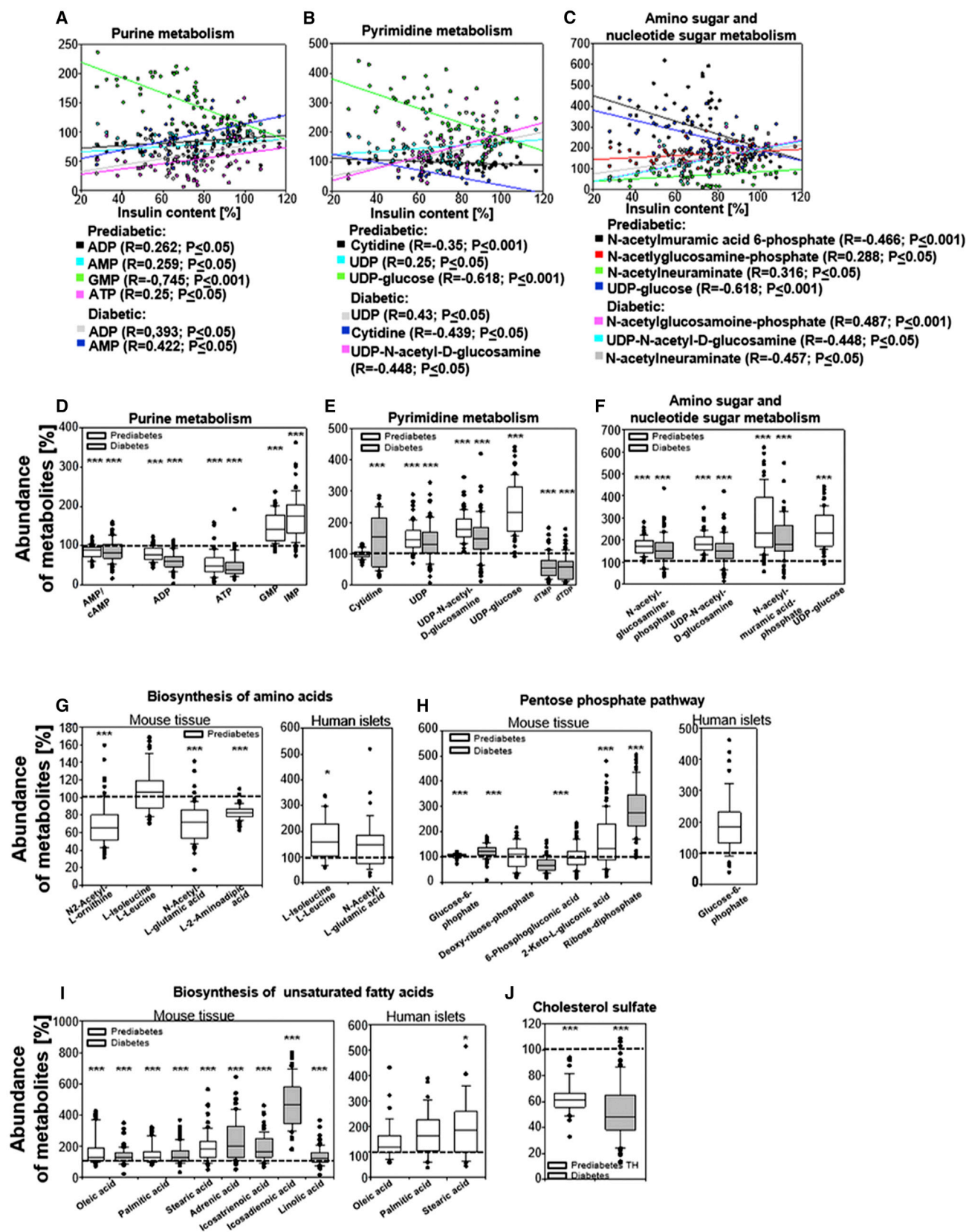


**Figure 3. Correlation Networks and Pathway Analysis of Prediabetic and Diabetic Disease States**

Prediabetic (A) and diabetic (B) core networks of metabolites demonstrating the involvement of multiple pathways and metabolites in T2D progression.



(legend on next page)

acetylcarnitine is a secretagogue for insulin, whereas stearyl-carnitine impairs insulin synthesis.

Insulin production is an energy-dependent process (Prentki et al., 2013). We investigated the relationship between the stearyl-carnitine accumulation in mice LHIs and the compounds of energy metabolism. In mouse tissues, stearyl-carnitine accumulation was negatively correlated with the abundances of ADP, ATP, triphosphate, and pyrophosphate, demonstrating a relationship between stearyl-carnitine and energy metabolism, especially oxidative phosphorylation (OxPhos; Figure 5I). In contrast, acetylcarnitine was not correlated with the abundances of those molecules. We investigated the influence of those two acylcarnitines on energy metabolism in a seahorse extracellular flux analyzer and found that stearyl-carnitine impaired mitochondrial energy metabolism, in particular glucose-stimulated respiration, while acetylcarnitine had minor effects (Figure 5J).

The OxPhos metabolites that were negatively correlated with stearyl-carnitine (Figure 5I) were positively correlated with the insulin content of the LHIs (Figure 6A). Those metabolites were less abundant in the diseased LHIs than in non-diabetic controls (Figures 6A and 6B). Compared to controls, the LHIs of PD mice had significantly lower ADP and ATP levels and decreased ATP/ADP ratio (Figure 6B), which is a critical parameter of cellular energy status and consumption (Metallo and Vander Heiden, 2013; Veech et al., 1979; Yuan et al., 2013). ADP and ATP are strongly associated with OxPhos. To gain more information on the respiratory chain complexes, we assessed *in situ* proteome profiles of LHIs in consecutive sections of the same pancreatic tissues used for metabolite profiling. The expression of several respiratory chain-associated proteins was significantly altered between diseased and control tissues. Those proteins were mostly upregulated in the diseased tissues and were negatively correlated with the insulin content, confirming their direct involvement in  $\beta$  cell pathophysiology (Figures 6C–6E). We expected that the observed changes would be reflected by morphological alterations of the mitochondria, so we examined the ultrastructural morphology of mitochondria in  $\beta$  cells from both mouse models and found reduced cristae numbers in PD mice and additional mitochondrial swelling in D mice (Figure 6F). Cholesterol sulfate was less abundant in the PD and D mice than in controls (Figure 4J). As cholesterol sulfate is a known stabilizing compound for membranes (Strott and Higashi, 2003), the lack of cholesterol sulfate might contribute to the morphological phenotype of the mitochondria.

Stearyl-carnitine and succinate levels were negatively correlated in the  $\beta$  cells, linking stearyl-carnitine accumulation to an impaired tricarboxylic acid (TCA) cycle (Figures 6G–6I). The

same functional link was proposed for skeletal muscle under insulin-resistant conditions and is consistent with the depletion of TCA intermediates, suggesting that  $\beta$ -oxidation does not match TCA (An et al., 2004; Koves et al., 2005, 2008; Muoio et al., 2012). Our results suggested that a link between stearyl-carnitine accumulation and the TCA cycle is also involved in T2D progression.

In summary, we showed that stearyl-carnitine accumulation in  $\beta$  cells impairs energy metabolism, OxPhos, the TCA cycle, and insulin synthesis, whereas acetylcarnitine functions as a secretagogue for insulin. Thus, both acylcarnitines foster  $\beta$  cell dysfunction.

### Accumulation of N-acyl Taurines Enhances Insulin Secretion

We detected N-acyl taurines in LHIs. Until now they had been detected only in the central nervous system, testes, kidney, liver, plasma, brown and white adipose tissue, heart, spleen, and lung of mice (Long et al., 2011; Saghatelian et al., 2004). N-acyl taurines are FAs conjugated to amino acids (Tan et al., 2010), and their physiological functions have remained elusive. In our metabolic core networks, N-acyl taurines had multiple correlations in both disease states, implicating multiple dependencies (Figures 3A and 3B). N-linoleoyl, N-ornithyl, N-stearyl, and N-oleoyl taurine were negatively correlated with insulin in LHIs of diseased mice, and they accumulated in LHIs of both PD and D mice (Figures 7A and 7B). N-palmitoyl taurine was reduced in PD mice and unchanged in D mice relative to that in controls (Figure 7A) and, furthermore, correlated with thiamine pyrophosphate in the TCA cycle ( $R = 0.265$ ;  $p \leq 0.05$ ), especially in the PD core network, suggesting that TCA depletion either causes N-acyl taurine formation or results from N-acyl taurine accumulation. In the D core network, N-stearyl taurine was correlated to cholesterol sulfate in the diabetes core network (Figure 3B). Of the five N-acyl-aurines that accumulated in mouse LHI, only N-palmitoyl taurine was detectable in human LHIs, where its pattern was similar to that in the mouse LHIs (Figures 7A and 7C).

FA amide hydrolase (FAAH) degrades N-acyl taurines in tissues (Saghatelian and Cravatt, 2005). We investigated the expression in mouse LHIs by immunohistochemistry (Figure S7) but did not detect a reduction in PD or D mice. Therefore, the observed N-acyl taurine accumulation was not an effect of deficient degradation.

We investigated the functional role of N-acyl taurine accumulation in the observed changes in  $\beta$  cells *in vitro* (Figures 7D–7H). N-oleoyl taurine and N-palmitoyl taurine were secretagogues for

**Figure 4. Selected Pathways that Directly Correlated with Insulin Content and Abundance of Metabolites in Selected Metabolic Pathways** (A–C) Correlation of pathways with insulin content. Purine metabolism (A). Pyrimidine metabolism (B). Amino sugar and nucleotide sugar metabolism (C).

(D) In purine metabolism, most components were less abundant in the disease states compared with those in non-diabetic controls.

(E) In pyrimidine metabolism, most components were more abundant in the disease states compared with those in non-diabetic controls.

(F) In amino sugar and nucleotide sugar metabolism, all detected metabolites were highly abundant.

(G) In biosynthesis of amino acids, most components were less abundant in mouse LHI. In LHIs isolated from humans with T2D, two components of this pathway were increased.

(H) Pentose phosphate pathway components varied in abundance in mouse LHI. In LHIs isolated from humans with T2D, glucose-phosphate was increased.

(I) In biosynthesis of unsaturated FA, the composition of FA changed with disease progression in mice, and all of the components were more abundant than in non-diabetic controls. In LHIs isolated from humans with T2D, oleic, palmitic, and stearic acid were increased.

(J) Abundance of cholesterol sulfate. All data were normalized to non-diabetic control (dashed line) and are presented as the mean  $\pm$  SEM.

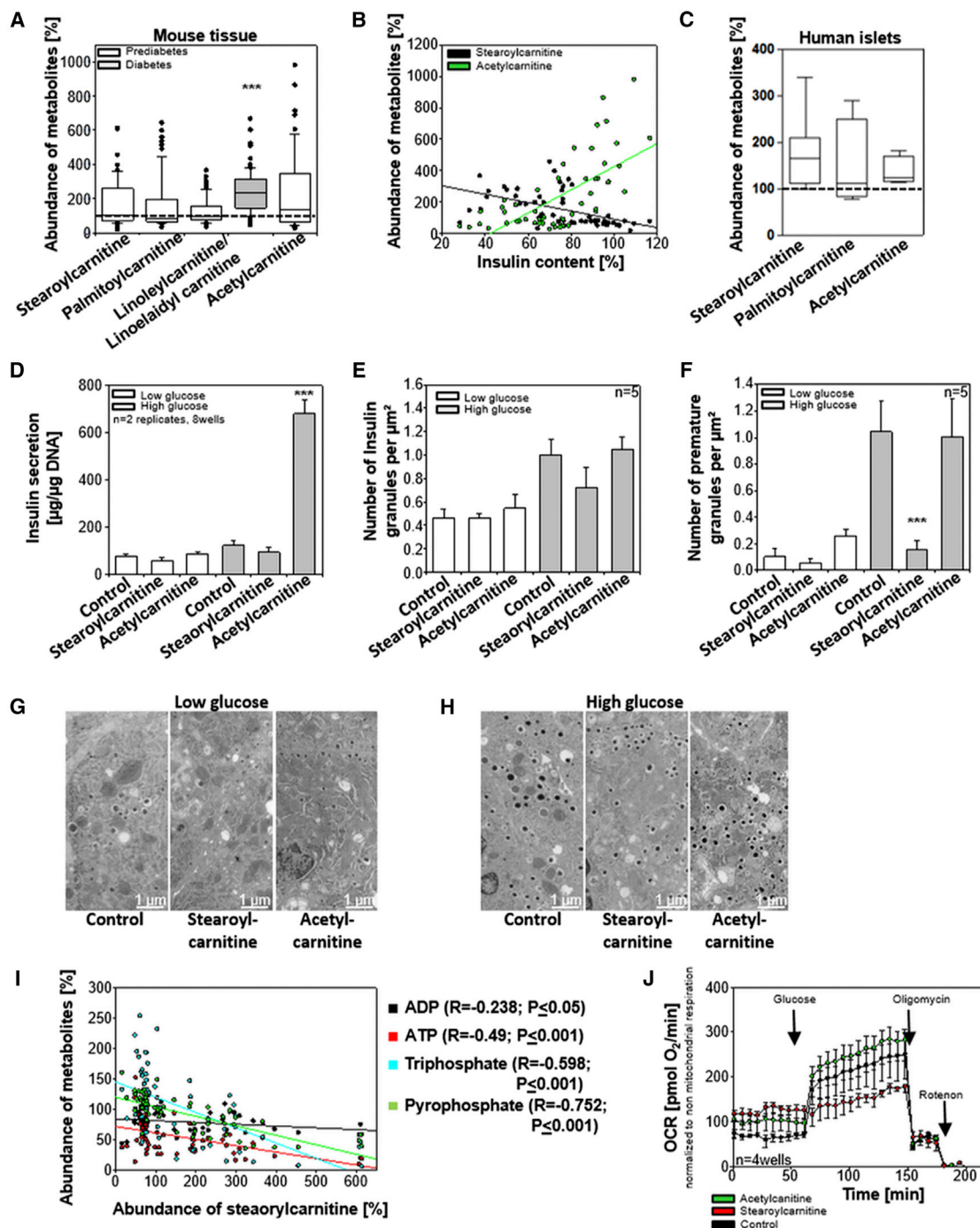


**Figure 5. Acylcarnitine Accumulation Impairs Insulin Synthesis and Exocytosis**

(A) Various acylcarnitines and acetylcarnitine accumulated predominantly in the PD disease state.  
 (B) Correlation of insulin content with stearoylcarnitine and acetylcarnitine abundance in mouse LHIs.  
 (C) Accumulation of stearoylcarnitine, palmitoylcarnitine, and acetylcarnitine in LHIs from human T2D donors.  
 (D) Insulin secretion was highly increased in cells treated with acetylcarnitine under high-glucose conditions.  
 (E) Quantification by transmission electron microscopy of all insulin granules in cells under different treatments.  
 (F) Quantification of numbers of premature insulin granules in cells under different treatments. Cells treated with stearoylcarnitine demonstrated a reduction of premature insulin granules under high-glucose conditions; acetylcarnitine treatment did not alter the number of premature insulin granules.  
 (G and H) Transmission electron micrographs of Min6 cells under low-glucose (G) and high-glucose (H) conditions (4,000 $\times$ , scale bar, 1  $\mu$ m).

(legend continued on next page)

insulin under both low- and high-glucose conditions, whereas N-stearoyl taurine did not affect insulin secretion (Figure 7D). Transmission electron microscopy revealed that treatment with N-oleoyl taurine or N-palmitoyl taurine reduced the total number of insulin granules (Figures 7E, 7G, and 7H) but did not change the number of premature insulin granules (Figures 7F–7H). Thus, N-acyl taurines did not influence insulin synthesis, but N-oleoyl taurine and N-palmitoyl taurine enhanced the secretion of mature insulin granules.

### **β Cell Dysfunction Results from Acylcarnitine and N-acyl Taurine Accumulation**

We developed a model of potential mechanisms contributing to the onset of β cell dysfunction in T2D (Figure 7I). Circulating FAs fuel β-oxidation for energy production (Figure 7I, step 1) via the carnitine shuttle (CPT1, CPT2; Figure 7I, step 2) into the mitochondrial matrix (McGarry, 2002; Prentki et al., 2013; Saponaro et al., 2015; Schooneman et al., 2013). FA overload of the mitochondria leads to excessive β-oxidation (Figure 7I, step 3) and acylcarnitine accumulation (Schooneman et al., 2013).

Acylcarnitines accumulate in LHIs (Figure 7I, steps 4 and 5). Acetylcarnitine leads to enhanced insulin secretion (Figure 7I, step 4), while stearoylcarnitine accumulation impairs the energy supply of β cells via TCA cycle depletion and OxPhos impairment (Figure 7I, steps 5, 6, and 7). Insulin production and processing are energy dependent (Prentki et al., 2013), so the energy deficiency might hamper the synthesis of insulin granules (Figure 7I, step 7). Accumulated N-oleoyl and N-palmitoyl taurines in β cells function as secretagogues for insulin (Figure 7I, step 8).

Thus, β cell dysfunction during T2D progression results from an imbalance of insulin synthesis and secretion caused by acylcarnitine and N-acyl taurine accumulation.

## **DISCUSSION**

We performed a comprehensive in situ-omics analysis of a large number of well-characterized LHIs in their intact immediate environment directly in pancreatic tissue. We focused on the consistent molecular changes in LHIs in two mouse models of T2D to exclude genotype-specific results but cover general disease-related aspects. Using a combination of MALDI-MSI analytics and a systems biological approach, we created a global map of the molecules associated with T2D progression and β cell dysfunction. Those data were supported by in situ metabolomics data from LHIs isolated from healthy humans and patients with T2D and by in vitro functional studies. N-acyl taurines were not previously recognized in LHIs, but our results showed that they are associated with early functional alterations. Furthermore, our data demonstrate that acylcarnitines were also involved in early functional alterations.

Ultrastructural data from β cells of PD and D mice demonstrated a severe reduction of insulin granules during T2D pro-

gression (Figure 1). The reduction was likely caused by an arrest of insulin synthesis rather than impaired insulin processing, as electron microscopic data revealed a shortage of premature insulin granules already in the PD mice (Figure 1). A similar reduction of insulin granules was reported in an ultrastructural morphometric analysis of human T2D (Masini et al., 2012). Other reports showed that insulin secretion is reduced in PD and in T2D (Cheng et al., 2013; Porte and Kahn, 2001).

Several metabolic pathways were altered in relation to T2D progression and β cell dysfunction (Figure 3). A recent transcriptomic analysis of LHIs from PD and D diet-induced obesity (DIO) mice reported several alterations in metabolic pathways, including de novo pyrimidine deoxyribonucleotide biosynthesis (Pepin et al., 2016), which is comparable to our data. One of the most prominently altered pathways that directly correlated with insulin depletion in our study was pyrimidine metabolism (Figure 4B). Cytidine appears to play a central role in pyrimidine metabolism and was correlated with many other metabolites (Figure 3A). Previously, cytidine was identified as a relevant molecule in diabetic retinopathy and nephropathy (Xia et al., 2010, 2011), but its function in β cells remained poorly understood. Newgard, with collaboration from MacDonald, recently showed a decrease in IMP and an increase in adenylosuccinate (S-AMP) in insulinoma cells under glucose stimulation (Gooding et al., 2015), indicating that purine pathway intermediates play an important role in insulin secretion (Gooding et al., 2015). In this study, S-AMP treatment overcame the defect in glucose-induced exocytosis in β cells from a human patient with T2D (Gooding et al., 2015). Our in situ data from mouse LHIs revealed an increase in IMP in PD mice (Figure 4D). We did not detect an elevation in S-AMP levels. The conflicting results in our study and the previous study might be due to the different model systems used. Another recently reported study by these groups showed a novel signaling pathway from isocitrate and NADPH to SENP1, which amplified insulin secretion and rescued dysfunctional human β cells; the glucose-dependent amplification of insulin exocytosis required isocitrate flux through cytosolic NADP<sup>+</sup>-dependent isocitrate dehydrogenase and the generation of cytosolic NADPH and glutathione (Ferdoussi et al., 2015). Another study demonstrated a regulatory role of NADPH in the redox control of exocytosis (Ivarsson et al., 2005). In our study, citrate/isocitrate was elevated in the LHIs of PD mice (Figure 6H) and humans with T2D (Figure 6I), but we could not generate data for NADPH. Hence, we could not exclude the possibility that any of the previously proposed mechanisms played a role in our results.

Acylcarnitines accumulated in mouse and human LHIs, and stearoylcarnitine and acetylcarnitine correlated with the insulin content (Figure 5). In a recent study of isolated LHIs, 3-hydroxy-tetradecanoylcarnitine, a carnitine ester, accumulated after glucolipotoxic insult, while other acylcarnitines and acetylcarnitine decreased (Doliba et al., 2015). That contrasts with our results in intact, non-isolated mouse LHIs and isolated human LHIs.

(I) Correlation of stearoylcarnitine to energy metabolism related metabolites.

(J) Influence of stearoylcarnitine and acetylcarnitine on cellular bioenergetics determined with a Seahorse extracellular flux analyzer. Stearoylcarnitine impaired mitochondrial energy metabolism; acetylcarnitine had no influence. All data were normalized to non-diabetic controls (dashed lines) or normalized as indicated and represented as mean ± SEM.

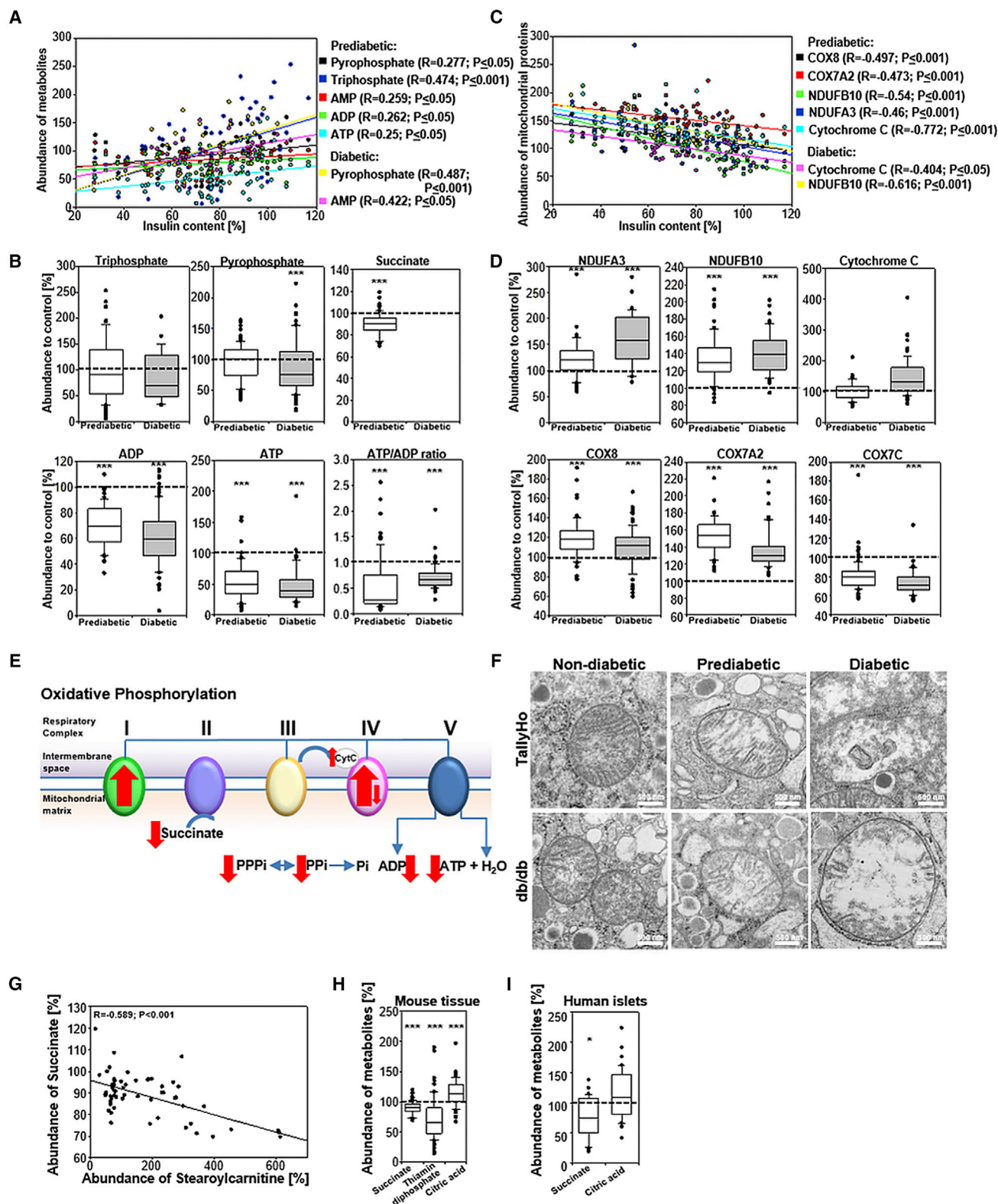


**Figure 6. Alterations in Energy Metabolism and Mitochondria**

(A) Pyrophosphate (PPi), triphosphate (PPPi), ADP, and ATP correlated positively with insulin content.

(B) The average abundances of PPi and PPPi were slightly reduced in prediabetes and significantly reduced in diabetes. ADP and ATP were significantly reduced in both disease states.

(legend continued on next page)

Although we did not detect 3-hydroxytetradecanoylcarnitine, we detected the accumulation of acetylcarnitine as well as that of several acylcarnitines (Figures 5A and 5C). The conflicting results between our study and the previous study might be due to the different model systems.

In the context of insulin resistance in skeletal muscle, overnutrition and FA overload of mitochondria is consistent with acylcarnitine accumulation and the depletion of TCA intermediates, suggesting that FA oxidation does not match TCA (Schooneman et al., 2013). Excessive  $\beta$ -oxidation in the presence of highly abundant FA could result in the acylcarnitine accumulation in LHs in our study (Figures 5A and 5C). Increased  $\beta$ -oxidation has been reported under diabetic conditions in LHs isolated from DIO mice (Pepin et al., 2016). Incomplete  $\beta$ -oxidation combined with acylcarnitine accumulation was observed in mitochondria isolated from insulin-resistant rat muscles (An et al., 2004; Koves et al., 2005). We detected a comparable situation in mouse LHs, where thiamine diphosphate and succinate levels, as well as succinate levels in human LHs, were reduced (Figures 6G–6I). Succinate is needed as a substrate for OxPhos and energy production. As ATP, one of the most important products of OxPhos, was strongly depleted (Figure 6B), it might be that there was too little succinate for OxPhos. Similar observations were made in association with obesity and T2D in patients and in insulin-resistant offspring of parents with diabetes (Morino et al., 2006; Muoio and Newgard, 2006; Ritov et al., 2010). Alterations of acylcarnitines' serum levels were recently described in patients under PD and T2D conditions and have been interpreted as markers of mitochondrial function (Mai et al., 2013). Our data clearly demonstrate that stearyl carnitine accumulation in  $\beta$  cells during T2D progression is linked to hampered insulin synthesis and energy deficiency via the TCA cycle and OxPhos (Figure 6).

The accumulation of N-acyl amino acids, especially N-acyl taurines, in LHs was integral to the process of  $\beta$  cell dysfunction (Figure 7). Research on those taurine-conjugated FAs has been limited, and their physiological role was unknown until now (Hanuš et al., 2014). Some of N-acyl taurines are able to activate TRP ion channels, thus enhancing  $\text{Ca}^{2+}$  influx into the cytoplasm (Waluk et al., 2013), which is a signal for insulin exocytosis (Henquin, 2009; Prentki, 1996). TRP channels are expressed in mouse primary tissues and rat LHs and  $\beta$  cells (Colsoul et al., 2011). Although not much is known about the expression of TRP channels in human tissue, several TRP channels were reported in the human pancreas, and some are specifically expressed in human LHs (Colsoul et al., 2011). Furthermore, mice deficient in *Trpm2* and *Trpm5* display a PD phenotype caused by  $\beta$  cell dysfunction (Colsoul et al., 2011). *Trpm2*<sup>−/−</sup> mice exhibit higher basal glucose levels and impaired glucose tolerance caused by lowered plasma insulin levels

(Uchida et al., 2011). Two independent laboratories described a similar phenotype for *Trpm5*<sup>−/−</sup> mouse (Colsoul et al., 2011). TRPM5 is involved in glucose-induced insulin release, and *Trpm5*<sup>−/−</sup> mice display impaired glucose tolerance caused by lower plasma insulin levels (Brixel et al., 2010; Colsoul et al., 2010). It might be possible that the enhanced insulin secretion under N-acyl taurine treatment observed in our study involves TRP channels.

In summary, our study is the first comprehensive analyses of in situ-omics data from LHs examined directly in tissues and analyzed using a systems biological approach, combined with data from humans and in vitro experiments. The onset of  $\beta$  cell dysfunction is an early event in T2D progression, as most of the detected alterations were already present in the PD state. There seem to be remarkable parallels between the mechanisms of insulin resistance in skeletal muscle and  $\beta$  cell dysfunction, which should be investigated further. Our data further point to insulin depletion as a result of a combination of hampered insulin refill and enhanced insulin granule release.

## STAR★METHODS

Detailed methods are provided in the online version of this paper and include the following:

- KEY RESOURCES TABLE
- CONTACT FOR REAGENT AND RESOURCE SHARING
- EXPERIMENTAL MODEL AND SUBJECT DETAILS
  - Mouse Models
  - Human Isolated Islets
  - Cell Lines
- METHOD DETAILS
  - Mouse Models: Body Weight and Blood Glucose
  - MALDI Imaging Mass Spectrometry
  - Annotation of Molecules
  - Insulin Secretion
  - DNA Content
  - Cellular Bioenergetics
  - Electron Microscopy
  - Immunofluorescence, Immunohistochemistry, and Image Analysis
- QUANTIFICATION AND STATISTICAL ANALYSIS
  - Bioinformatics, Statistical Analysis
  - Network Generation

## SUPPLEMENTAL INFORMATION

Supplemental Information includes seven figures and three tables and can be found with this article online at <http://dx.doi.org/10.1016/j.cmet.2017.04.012>.

(C) NDUFA3, NDUFB10, Cytochrome C, COX8, and COX7A2 were negatively correlated with insulin content.

(D) The expression of all analyzed mitochondrial proteins except Cytochrome C was highly altered.

(E) Graphical summary of alterations in oxidative phosphorylation. Proteins of respiratory chain complex I and complex IV were mainly upregulated under diseased conditions, except for COX7C. The metabolites from complex V were all less abundant under disease conditions than in non-diabetic controls.

(F) Electron micrographs of mitochondrial alterations in TallyHo and db/db mice during disease progression (magnification: 10,000 $\times$ , scale bar, 500 nm).

(G) Correlation of stearyl carnitine with succinate levels.

(H and I) Reduced abundance of components of TCA cycle in mouse tissues (H) and LHs isolated from human donors (I). All data were normalized to non-diabetic controls (dashed lines) and represented as mean  $\pm$  SEM.

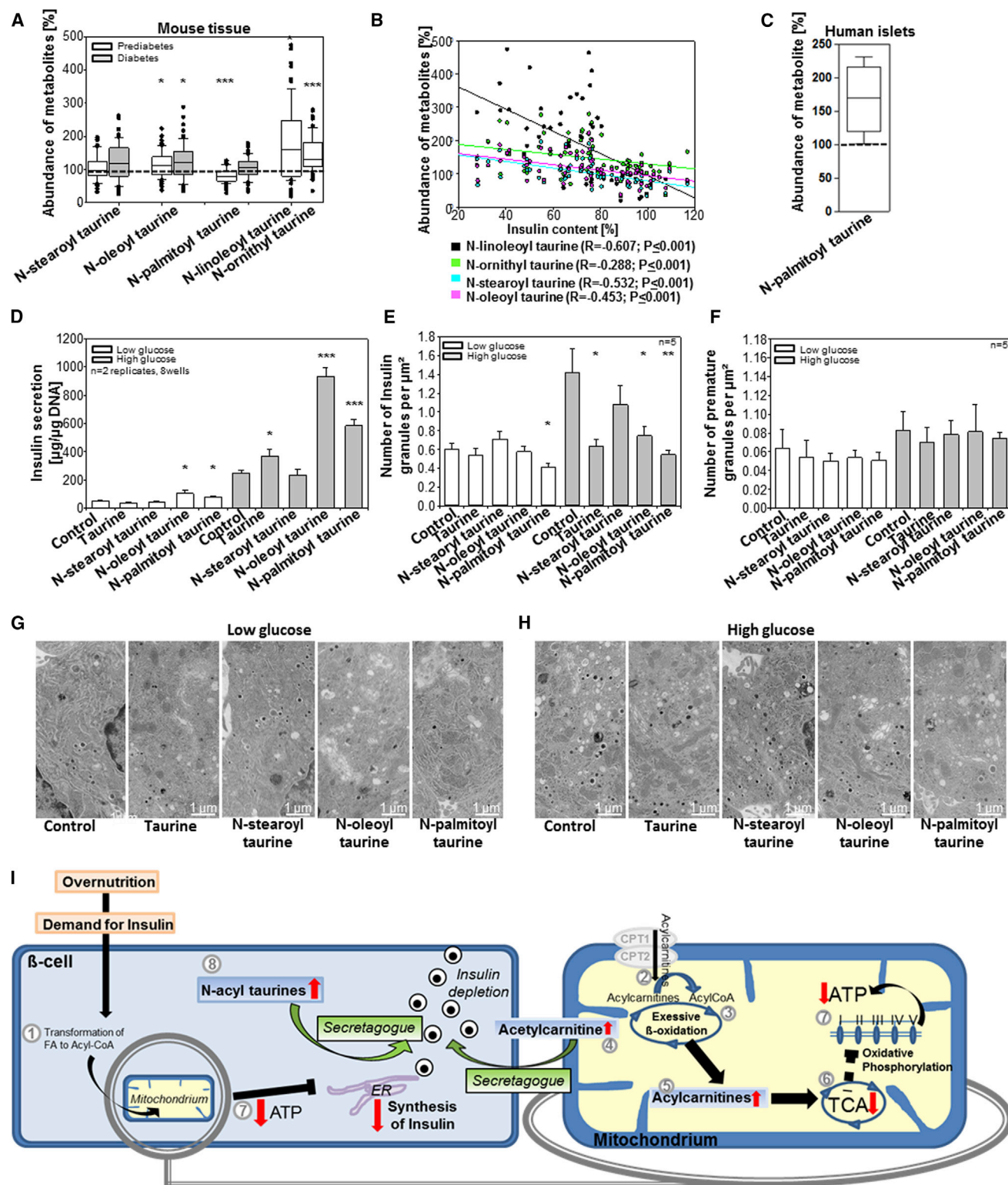


**Figure 7. Accumulation of Specific N-acyl Taurines Enhanced Insulin Secretion**

- (A) Accumulation of N-acyl taurines in LHIs of PD and D mice.  
 (B) N-acyl taurines correlated negatively with the insulin content of the LHIs.  
 (C) N-palmitoyl taurine accumulated in LHIs from patients with T2D.  
 (D) β cells treated with N-oleoyl taurine or N-palmitoyl taurine showed significantly enhanced insulin secretion under low- and high-glucose conditions.

(legend continued on next page)

## AUTHOR CONTRIBUTIONS

M.A. designed the study, carried out experiments, analyzed and interpreted results, and wrote the manuscript. D.B. carried out experiments and statistical analysis and edited the manuscript. N.S., A.F., and A.B. performed experiments. P.E.M., J.E.M.F., J.L., and P.E.L. provided human material and edited the manuscript. M.J. and S.K. performed cell experiments, interpreted results, and edited the manuscript. J.K. and N.S.M. performed statistical analysis and edited the manuscript. A.P. and T.A. performed data analysis. S.N. provided experimental animals and edited the manuscript. M.H.d.A. edited the manuscript. M.H.T. and A.W. discussed results and edited the manuscript.

## ACKNOWLEDGMENTS

This project was funded by the Ministry of Education and Research of the Federal Republic of Germany (BMBF; Grant No. 01ZX1310B), the Deutsche Forschungsgemeinschaft (Grant Nos. HO 1254/3-1, SFB 824 TP Z02) to A.W., and the German Center for Diabetes Research (DZD). This work was further funded in part by the European Horizon2020 Programme (Grant No. 634402) to T.A. and A.P. and the European Commission, FP7 grant MIMOMics (contract #305280). P.E.L. holds the Charles A. Allard Chair in Diabetes Research and is funded by the Canadian Institutes of Health Research. P.E.M. holds a 2016/2017 Killam Annual Professorship. Human islet isolation was supported by funding from the Alberta Diabetes Foundation. We thank Moya Wu for excellent assistance with experimental animals and Ulrike Buchholz, Claudia-Mareike Pflüger, Gabriele Mettenleiter, Manuel Pauling, and Andreas Voss for technical assistance.

Received: August 23, 2016

Revised: February 14, 2017

Accepted: April 13, 2017

Published: June 6, 2017

## REFERENCES

- Ahn, Y.B., Xu, G., Marselli, L., Toschi, E., Sharma, A., Bonner-Weir, S., Sgroi, D.C., and Weir, G.C. (2007). Changes in gene expression in beta cells after islet isolation and transplantation using laser-capture microdissection. *Diabetologia* 50, 334–342.
- Aichler, M., and Walch, A. (2015). MALDI imaging mass spectrometry: current frontiers and perspectives in pathology research and practice. *Lab. Invest.* 95, 422–431.
- An, J., Muoio, D.M., Shiota, M., Fujimoto, Y., Cline, G.W., Shulman, G.I., Koves, T.R., Stevens, R., Millington, D., and Newgard, C.B. (2004). Hepatic expression of malonyl-CoA decarboxylase reverses muscle, liver and whole-animal insulin resistance. *Nat. Med.* 10, 268–274.
- Brixel, L.R., Monteilh-Zoller, M.K., Ingenbrandt, C.S., Fleig, A., Penner, R., Enklaar, T., Zabel, B.U., and Prawitt, D. (2010). TRPM5 regulates glucose-stimulated insulin secretion. *Pflugers Arch.* 460, 69–76.
- Buck, A., Ly, A., Balluff, B., Sun, N., Gorzalka, K., Feuchtinger, A., Janssen, K.P., Kuppen, P.J., van de Velde, C.J., Weirich, G., et al. (2015). High-resolution MALDI-FT-ICR MS imaging for the analysis of metabolites from formalin-fixed, paraffin-embedded clinical tissue samples. *J. Pathol.* 237, 123–132.
- Cheng, K., Andrikopoulos, S., and Gunton, J.E. (2013). First phase insulin secretion and type 2 diabetes. *Curr. Mol. Med.* 13, 126–139.
- Colsohl, B., Schraenen, A., Lemaire, K., Quintens, R., Van Lommel, L., Segal, A., Owsianik, G., Talavera, K., Voets, T., Margolskee, R.F., et al. (2010). Loss of high-frequency glucose-induced Ca<sup>2+</sup> oscillations in pancreatic islets correlates with impaired glucose tolerance in *Trpm5*<sup>-/-</sup> mice. *Proc. Natl. Acad. Sci. USA* 107, 5208–5213.
- Colsohl, B., Vennekens, R., and Nilius, B. (2011). Transient receptor potential cation channels in pancreatic  $\beta$  cells. *Rev. Physiol. Biochem. Pharmacol.* 161, 87–110.
- Dalton, A.J. (1952). Preparation of tissue sections for electron microscopy. *Methods Med. Res.* 5, 234–241.
- do Amaral, A.S., Pawlick, R.L., Rodrigues, E., Costal, F., Pepper, A., Galvão, F.H., Correa-Giannella, M.L., and Shapiro, A.M. (2013). Glutathione ethyl ester supplementation during pancreatic islet isolation improves viability and transplant outcomes in a murine marginal islet mass model. *PLoS ONE* 8, e55288.
- Doliba, N.M., Liu, Q., Li, C., Chen, J., Chen, P., Liu, C., Frederick, D.W., Baur, J.A., Bennett, M.J., Naji, A., and Matschinsky, F.M. (2015). Accumulation of 3-hydroxytetradecenoic acid: cause or corollary of glucolipotoxic impairment of pancreatic  $\beta$ -cell bioenergetics? *Mol. Metab.* 4, 926–939.
- Ferdaoussi, M., Dai, X., Jensen, M.V., Wang, R., Peterson, B.S., Huang, C., Ilkayeva, O., Smith, N., Miller, N., Hajmrl, C., et al. (2015). Isocitrate-to-SEN1 signaling amplifies insulin secretion and rescues dysfunctional  $\beta$  cells. *J. Clin. Invest.* 125, 3847–3860.
- Gooding, J.R., Jensen, M.V., Dai, X., Wenner, B.R., Lu, D., Arumugam, R., Ferdaoussi, M., MacDonald, P.E., and Newgard, C.B. (2015). Adenylosuccinate is an insulin secretagogue derived from glucose-induced purine metabolism. *Cell Rep.* 13, 157–167.
- Hanuš, L., Shohami, E., Bab, I., and Mechoulam, R. (2014). N-Acyl amino acids and their impact on biological processes. *Biofactors* 40, 381–388.
- Henquin, J.C. (2009). Regulation of insulin secretion: a matter of phase control and amplitude modulation. *Diabetologia* 52, 739–751.
- Irving-Rodgers, H.F., Choong, F.J., Hummitzsch, K., Parish, C.R., Rodgers, R.J., and Simeonovic, C.J. (2014). Pancreatic islet basement membrane loss and remodeling after mouse islet isolation and transplantation: impact for allograft rejection. *Cell Transplant.* 23, 59–72.
- Ivarsson, R., Quintens, R., Dejonghe, S., Tsukamoto, K., in 't Veld, P., Renström, E., and Schuit, F.C. (2005). Redox control of exocytosis: regulatory role of NADPH, thioredoxin, and glutaredoxin. *Diabetes* 54, 2132–2142.
- Kim, J.H., Sen, S., Avery, C.S., Simpson, E., Chandler, P., Nishina, P.M., Churchill, G.A., and Naggert, J.K. (2001). Genetic analysis of a new mouse model for non-insulin-dependent diabetes. *Genomics* 74, 273–286.
- Konstantopoulos, N., Molero, J.C., McGee, S.L., Spolding, B., Connor, T., de Vries, M., Wanyonyi, S., Fahey, R., Morrison, S., Swinton, C., et al. (2012). Methazolamide is a new hepatic insulin sensitizer that lowers blood glucose in vivo. *Diabetes* 61, 2146–2154.
- Koves, T.R., Li, P., An, J., Akimoto, T., Slentz, D., Ilkayeva, O., Dohm, G.L., Yan, Z., Newgard, C.B., and Muoio, D.M. (2005). Peroxisome proliferator-activated receptor-gamma co-activator 1 $\alpha$ -mediated metabolic remodeling of skeletal myocytes mimics exercise training and reverses lipid-induced mitochondrial inefficiency. *J. Biol. Chem.* 280, 33588–33598.
- Koves, T.R., Ussher, J.R., Noland, R.C., Slentz, D., Mosedale, M., Ilkayeva, O., Bain, J., Stevens, R., Dyck, J.R., Newgard, C.B., et al. (2008). Mitochondrial overload and incomplete fatty acid oxidation contribute to skeletal muscle insulin resistance. *Cell Metab.* 7, 45–56.
- Krumsiek, J., Suhre, K., Illig, T., Adamski, J., and Theis, F.J. (2011). Gaussian graphical modeling reconstructs pathway reactions from high-throughput metabolomics data. *BMC Syst. Biol.* 5, 21.
- Krumsiek, J., Suhre, K., Evans, A.M., Mitchell, M.W., Mohney, R.P., Milburn, M.V., Wägele, B., Römisch-Margl, W., Illig, T., Adamski, J., et al. (2012). Mining the unknown: a systems approach to metabolite identification combining genetic and metabolic information. *PLoS Genet.* 8, e1003005.
- Liang, Y., Arakawa, K., Ueta, K., Matsushita, Y., Kuriyama, C., Martin, T., Du, F., Liu, Y., Xu, J., Conway, B., et al. (2012). Effect of canagliflozin on renal threshold for glucose, glycemia, and body weight in normal and diabetic animal models. *PLoS ONE* 7, e30555.

(E) The total number of insulin granules in  $\beta$  cells under treatment with N-oleoyl taurine or N-palmitoyl taurine was significantly reduced.

(F) The number of premature insulin granules under N-acyl taurines treatment was unaltered.

(G and H) Electron micrographs of Min6 cells under low-glucose (G) and high-glucose (H) conditions.

(I) Proposed mechanism for LHI dysfunction in T2D. All data were normalized to non-diabetic controls (dashed lines) and represented as mean  $\pm$  SEM.

- Long, J.Z., LaCava, M., Jin, X., and Cravatt, B.F. (2011). An anatomical and temporal portrait of physiological substrates for fatty acid amide hydrolase. *J. Lipid Res.* 52, 337–344.
- Lyon, J., Manning Fox, J.E., Spigelman, A.F., Kim, R., Smith, N., O’Gorman, D., Kin, T., Shapiro, A.M., Rajotte, R.V., and MacDonald, P.E. (2016). Research-focused isolation of human islets from donors with and without diabetes at the Alberta Diabetes Institute IsletCore. *Endocrinology* 157, 560–569.
- Mai, M., Tönjes, A., Kovacs, P., Stumvoll, M., Fiedler, G.M., and Leichtle, A.B. (2013). Serum levels of acylcarnitines are altered in prediabetic conditions. *PLoS ONE* 8, e82459.
- Maier, S.K., Hahne, H., Gholami, A.M., Balluff, B., Meding, S., Schoene, C., Walch, A.K., and Kuster, B. (2013). Comprehensive identification of proteins from MALDI imaging. *Mol. Cell. Proteomics* 12, 2901–2910.
- Mantini, D., Petrucci, F., Pieragostino, D., Del Boccio, P., Di Nicola, M., Di Ilio, C., Federici, G., Sacchetta, P., Comani, S., and Urbani, A. (2007). LIMPIC: a computational method for the separation of protein MALDI-TOF-MS signals from noise. *BMC Bioinformatics* 8, 101.
- Marciniak, A., Cohrs, C.M., Tsata, V., Chouinard, J.A., Selck, C., Stertmann, J., Reichelt, S., Rose, T., Ehehalt, F., Weitz, J., et al. (2014). Using pancreas tissue slices for in situ studies of islet of Langerhans and acinar cell biology. *Nat. Protoc.* 9, 2809–2822.
- Masini, M., Marselli, L., Bugliani, M., Martino, L., Masiello, P., Marchetti, P., and De Tata, V. (2012). Ultrastructural morphometric analysis of insulin secretory granules in human type 2 diabetes. *Acta Diabetol.* 49 (Suppl 1), S247–S252.
- McDonnell, L.A., van Remoortere, A., de Velde, N., van Zeijl, R.J., and Deelder, A.M. (2010). Imaging mass spectrometry data reduction: automated feature identification and extraction. *J. Am. Soc. Mass Spectrom.* 21, 1969–1978.
- McGarry, J.D. (2002). Banting lecture 2001: dysregulation of fatty acid metabolism in the etiology of type 2 diabetes. *Diabetes* 51, 7–18.
- Metallo, C.M., and Vander Heiden, M.G. (2013). Understanding metabolic regulation and its influence on cell physiology. *Mol. Cell* 49, 388–398.
- Morini, S., Braun, M., Onori, P., Cicalese, L., Elias, G., Gaudio, E., and Rastellini, C. (2006). Morphological changes of isolated rat pancreatic islets: a structural, ultrastructural and morphometric study. *J. Anat.* 209, 381–392.
- Morino, K., Petersen, K.F., and Shulman, G.I. (2006). Molecular mechanisms of insulin resistance in humans and their potential links with mitochondrial dysfunction. *Diabetes* 55 (Suppl 2), S9–S15.
- Muoio, D.M., and Newgard, C.B. (2006). Obesity-related derangements in metabolic regulation. *Annu. Rev. Biochem.* 75, 367–401.
- Muoio, D.M., Noland, R.C., Kovalik, J.P., Seiler, S.E., Davies, M.N., DeBalsi, K.L., Ilkayeva, O.R., Stevens, R.D., Kheterpal, I., Zhang, J., et al. (2012). Muscle-specific deletion of carnitine acetyltransferase compromises glucose tolerance and metabolic flexibility. *Cell Metab.* 15, 764–777.
- Negi, S., Jetha, A., Aikin, R., Hasilo, C., Sladek, R., and Paraskevas, S. (2012). Analysis of beta-cell gene expression reveals inflammatory signaling and evidence of dedifferentiation following human islet isolation and culture. *PLoS ONE* 7, e30415.
- Norris, J.L., and Caprioli, R.M. (2013). Analysis of tissue specimens by matrix-assisted laser desorption/ionization imaging mass spectrometry in biological and clinical research. *Chem. Rev.* 113, 2309–2342.
- Pepin, É., Al-Mass, A., Attané, C., Zhang, K., Lamontagne, J., Lussier, R., Madiraju, S.R., Joly, E., Ruderman, N.B., Sladek, R., et al. (2016). Pancreatic  $\beta$ -cell dysfunction in diet-induced obese mice: roles of AMP-kinase, protein kinase C $\epsilon$ , mitochondrial and cholesterol metabolism, and alterations in gene expression. *PLoS ONE* 11, e0153017.
- Poitout, V., and Robertson, R.P. (2008). Glucolipotoxicity: fuel excess and beta-cell dysfunction. *Endocr. Rev.* 29, 351–366.
- Porte, D., Jr., and Kahn, S.E. (2001). Beta-cell dysfunction and failure in type 2 diabetes: potential mechanisms. *Diabetes* 50 (Suppl 1), S160–S163.
- Prentki, M. (1996). New insights into pancreatic beta-cell metabolic signaling in insulin secretion. *Eur. J. Endocrinol.* 134, 272–286.
- Prentki, M., Matschinsky, F.M., and Madiraju, S.R.M. (2013). Metabolic signaling in fuel-induced insulin secretion. *Cell Metab.* 18, 162–185.
- Rajotte, R.V., Evans, M.G., Warnock, G.L., and Kneteman, N.M. (1990). Islet cryopreservation. *Horm. Metab. Res. Suppl.* 25, 72–81.
- Ritov, V.B., Menshikova, E.V., Azuma, K., Wood, R., Toledo, F.G.S., Goodpaster, B.H., Ruderman, N.B., and Kelley, D.E. (2010). Deficiency of electron transport chain in human skeletal muscle mitochondria in type 2 diabetes mellitus and obesity. *Am. J. Physiol. Endocrinol. Metab.* 298, E49–E58.
- Saghatelian, A., and Cravatt, B.F. (2005). Discovery metabolite profiling—forging functional connections between the proteome and metabolome. *Life Sci.* 77, 1759–1766.
- Saghatelian, A., Trauger, S.A., Want, E.J., Hawkins, E.G., Siuzdak, G., and Cravatt, B.F. (2004). Assignment of endogenous substrates to enzymes by global metabolite profiling. *Biochemistry* 43, 14332–14339.
- Saponaro, C., Gaggini, M., Carli, F., and Gastaldelli, A. (2015). The subtle balance between lipolysis and lipogenesis: a critical point in metabolic homeostasis. *Nutrients* 7, 9453–9474.
- Schooneman, M.G., Vaz, F.M., Houten, S.M., and Soeters, M.R. (2013). Acylcarnitines: reflecting or inflicting insulin resistance? *Diabetes* 62, 1–8.
- Shin, S.Y., Fauman, E.B., Petersen, A.K., Krumsiek, J., Santos, R., Huang, J., Arnold, M., Erte, I., Forgetta, V., Yang, T.P., et al.; Multiple Tissue Human Expression Resource (MuTHER) Consortium (2014). An atlas of genetic influences on human blood metabolites. *Nat. Genet.* 46, 543–550.
- Strott, C.A., and Higashi, Y. (2003). Cholesterol sulfate in human physiology: what’s it all about? *J. Lipid Res.* 44, 1268–1278.
- Sun, N., Ly, A., Meding, S., Witting, M., Hauck, S.M., Ueffing, M., Schmitt-Kopplin, P., Aichler, M., and Walch, A. (2014). High-resolution metabolite imaging of light and dark treated retina using MALDI-FTICR mass spectrometry. *Proteomics* 14, 913–923.
- Sun, N., Fernandez, I.E., Wei, M., Wu, Y., Aichler, M., Eickelberg, O., and Walch, A. (2016). Pharmacokinetic and pharmacometabolomic study of pirfenidone in normal mouse tissues using high mass resolution MALDI-FTICR-mass spectrometry imaging. *Histochem. Cell Biol.* 145, 201–211.
- Tan, B., O’Dell, D.K., Yu, Y.W., Monn, M.F., Hughes, H.V., Burstein, S., and Walker, J.M. (2010). Identification of endogenous acyl amino acids based on a targeted lipidomics approach. *J. Lipid Res.* 51, 112–119.
- Uchida, K., Dezaki, K., Damdindorj, B., Inada, H., Shiuchi, T., Mori, Y., Yada, T., Minokoshi, Y., and Tominaga, M. (2011). Lack of TRPM2 impaired insulin secretion and glucose metabolisms in mice. *Diabetes* 60, 119–126.
- Veech, R.L., Lawson, J.W., Cornell, N.W., and Krebs, H.A. (1979). Cytosolic phosphorylation potential. *J. Biol. Chem.* 254, 6538–6547.
- Waluk, D.P., Vielfort, K., Derakhshan, S., Aro, H., and Hunt, M.C. (2013). N-Acyl taurines trigger insulin secretion by increasing calcium flux in pancreatic  $\beta$ -cells. *Biochem. Biophys. Res. Commun.* 430, 54–59.
- Xia, J.F., Hu, P., Liang, Q.L., Zou, T.T., Wang, Y.M., and Luo, G.A. (2010). Correlations of creatine and six related pyrimidine metabolites and diabetic nephropathy in Chinese type 2 diabetic patients. *Clin. Biochem.* 43, 957–962.
- Xia, J.F., Wang, Z.H., Liang, Q.L., Wang, Y.M., Li, P., and Luo, G.A. (2011). Correlations of six related pyrimidine metabolites and diabetic retinopathy in Chinese type 2 diabetic patients. *Clin. Chim. Acta* 412, 940–945.
- Yuan, H.X., Xiong, Y., and Guan, K.L. (2013). Nutrient sensing, metabolism, and cell growth control. *Mol. Cell* 49, 379–387.

## STAR★METHODS

### KEY RESOURCES TABLE

REAGENT or RESOURCE	SOURCE	IDENTIFIER
<b>Antibodies</b>		
Polyclonal guinea pig anti-insulin	Dako	A0564; RRID: AB_10013624
Polyclonal rabbit anti-glucagon	Abcam	ab8055; RRID: AB_2247265
Polyclonal goat anti-PDX1	Abcam	ab47383; RRID: AB_2162359
Rabbit anti-CPT1a	Acris Antibodies	TA323382
Rabbit anti-CPT2	Abcam	ab181114
Rabbit anti-fatty acid amide hydrolase	Abcam	ab128917; RRID: AB_11144330
<b>Biological Samples</b>		
Human islets	Alberta Diabetes Institute Islet Core	N/A
<b>Chemicals, Peptides, and Recombinant Proteins</b>		
9-aminoacridine hydrochloride monohydrate	Sigma-Aldrich	A38401
Sinapic acid	Sigma-Aldrich	D7927
Acetonitrile	Sigma-Aldrich	270717
Trifluoroacetic acid	Sigma-Aldrich	91700
Stearoyl-L-carnitine	Sigma-Aldrich	61229
N-Stearoyl Taurine	Cayman Chemical	Cay-10005610
L-Acetylcarnitine	Cayman Chemical	Cay-16948
N-Oleoyl Taurine	Cayman Chemical	10005609
N-Palmitoyl Taurine	Cayman Chemical	10005611
<b>Critical Commercial Assays</b>		
Mouse Ultrasensitive Insulin ELISA	ALPCO	80-INSMSU-E01
Quant-it Picogreen dsDNA Assay	Life Technologies	P7589
<b>Deposited Data</b>		
Metabolite imaging of islets	MALDI imaging mass spectrometry	<a href="http://dx.doi.org/10.15134/2017M0001">http://dx.doi.org/10.15134/2017M0001</a>
<b>Experimental Models: Cell Lines</b>		
MIN6	Osaka University, Japan	Prof. J. Miyazaki
<b>Experimental Models: Organisms/Strains</b>		
Mouse: BKS.Cg- <i>Dock7</i> <sup>m+/+</sup> <i>Lepr</i> <sup>db</sup> /J	The Jackson Laboratory	000642
Mouse: TallyHo/JngJ	The Jackson Laboratory	005314
<b>Software and Algorithms</b>		
SmartFormula	Bruker Daltonik GmbH	SmartFormula
MATLAB	MathWorks	R2013a
Definiens TissueStudio3	Definiens AG	Definiens TissueStudio3
FlexImaging 4.0	Bruker Daltonik GmbH	FlexImaging 4.0
ClinProTools	Bruker Daltonik GmbH	ClinProTools
FlexControl 3.0	Bruker Daltonik GmbH	FlexControl 3.0

### CONTACT FOR REAGENT AND RESOURCE SHARING

Further information and requests for resources and reagents should be directed to and will be fulfilled by the Lead Contact, [axel.walch@helmholtz-muenchen.de](mailto:axel.walch@helmholtz-muenchen.de).

### EXPERIMENTAL MODEL AND SUBJECT DETAILS

#### Mouse Models

This study included two T2D mouse models. One part of the analysis was conducted in male BKS.Cg-*Dock7*<sup>m+/+</sup> *Lepr*<sup>db</sup>/J (db/db) mice, the most popular, and well-characterized animal model for diabetes and obesity ([Konstantopoulos et al., 2012](#); [Liang et al.,](#)

2012). The db/db mouse develops “monogenic” obesity due to a single spontaneous gene mutation (*Lep<sup>db</sup>*; db/db). Male db/db mice that were fed a high-fat diet started to develop obesity at 4 weeks of age, expressed a modest increase in random-fed blood glucose concentrations at the age of 5 weeks and quickly progressed to pronounced hyperglycemia at the age of 6 weeks (Figure S1). Overtly diabetic db/db mice, displaying average random-fed blood glucose concentrations of approximately 500 mg/dl for 4 consecutive weeks, as well as age-matched, non-diabetic, lean, male control littermates (Dock7<sup>m</sup> +/Dock7<sup>m</sup> +) were sacrificed at 9 weeks of age (Figure S1). A second cohort of younger db/db mice, expressing only modestly elevated random-fed blood glucose concentrations (< 250 mg/dl), was sacrificed 6 weeks of age (Figure S1). These animals are termed prediabetic throughout the manuscript (Figure S1).

A second set of analyses was conducted in an alternative murine diabetes model, the male TallyHo/JngJ (TallyHo) mouse, which originates from two outbred Theiler Original mice displaying polyuria and glucosuria. The TallyHo model is thought to recapitulate broader aspects of human “diabetes” than the db/db model as its obese and diabetic pathophenotype is driven by various diabetes-susceptibility alleles (Kim et al., 2001). When compared with those in male db/db mice, the onset and progression of hyperglycemia in male TallyHo are more variable and delayed, and the pathophenotype is less than 100% penetrant. The selected male TallyHo mice started to develop obesity at 4 weeks of age and hyperglycemia was more variable and less rapid in those mice than in db/db males (Figure S1). The two closest lean relatives of TallyHo mice share only 86.8% of the TallyHo genotype. Therefore, we decided to compare obese, diabetic TallyHo males with age-matched obese, non-diabetic littermate controls. For that purpose, we fed one subset of TallyHo males a starch-free and saccharose-free high-fat diet, which resulted in obesity similar to that in the mice fed a high-fat diet but prevented the onset of hyperglycemia (Figure S1). Obese, diabetic TallyHo mice, displaying average random-fed blood glucose concentrations of approximately 500 mg/dl for at least 4 consecutive weeks, and age-matched obese, non-diabetic TallyHo controls were sacrificed at 11 weeks of age (Figure S1). Another subset of TallyHo males expressing only a modest increase in random-fed blood glucose concentrations (< 250 mg/dl) was sacrificed at 7 weeks of age and are termed pre-diabetic throughout this manuscript.

All animals were bred and housed in a temperature-controlled and humidity-controlled environment in compliance with the protocols of the Federation of Laboratory Animal Science Associations. The Upper Bavarian government approved all animal experiments conducted in this study (Gz.55.2-1-54-2531-70-07, 55.2-1-2532-153-11). After weaning at 3 weeks of age, the mice were started on a high-fat diet (Ssniff Spezialdiäten, Soest, Germany) containing palm fat (13.5% of fat), sunflower oil (13.5%), starch (30%), saccharose (10%), casein (20%), lignocellulose (5%), mineral (5%) and vitamin mix (2%), safflower oil (0.5%), and linseed oil (0.5%). To prevent diabetes onset in diabetes-prone TallyHo mice, we used a high-fat diet lacking starch and saccharose but containing palm fat (33.5% of fat), sunflower oil (33.5%), casein (20%), lignocellulose (5%), mineral (5%) and vitamin mix (2%), safflower oil (0.5%), and linseed oil (0.5%; Ssniff Spezialdiäten, Soest, Germany).

### Human Isolated Islets

Human pancreata were obtained from cadaveric donors with the assistance of the Human Organ Procurement and Exchange (HOPE) program in Edmonton, Canada, together with the Trillium Gift of Life Network (<http://www.giftoflife.on.ca>), and Transplant Quebec (<http://www.transplantquebec.ca>). Islets were isolated via enzymatic digestion and gradient purification, as previously described (Lyon et al., 2016). Islet purity ranged from 75%–100%. The islets were subsequently cultured in CMRL 1066 (Corning, Tewksbury, MA, USA) supplemented with 0.5% BSA (Equitech-Bio, Kerrville, TX, USA), 1% Insulin-Transferrin-Selenium (Corning), 100 U/mL penicillin/streptomycin (Life Technologies, Burlington, ON, Canada) and L-glutamine (Sigma-Aldrich, Oakville, ON, Canada) prior to cryopreservation with stepwise addition of DMSO, as previous described (Rajotte et al., 1990). In this study 54 isolated Langerhans islets from three healthy human donors and three donors with T2D were included. To stay comparable to the mouse models, all human donors were male.

### Cell Lines

MIN6 cells, kindly provided by Prof. J. Miyazaki (Osaka University, Japan), were maintained in Dulbecco's modified Eagle's medium (DMEM) with glutaMAX containing 25 mM glucose (Thermo scientific), supplemented with 15% heat-inactivated hyclone serum (Thermo scientific), 72  $\mu$ M 2-mercaptoethanol (Roth, Germany), and 1% penicillin and streptomycin (Thermo scientific). Cells were incubated at 37°C in a humidified 5% CO<sub>2</sub>, 95% air environment.

## METHOD DETAILS

### Mouse Models: Body Weight and Blood Glucose

Once per week starting at 4 weeks of age, we measured body mass and collected blood samples from lateral tail veins of random-fed animals. Blood glucose was measured in full blood with a glucometer (Contour, Bayer Vital, Germany).

### MALDI Imaging Mass Spectrometry

#### MALDI-FT-ICR: Metabolite Imaging

Frozen mouse tissues or isolated human LHs were cryosectioned at 12  $\mu$ m (CM1950, Leica Microsystems, Wetzlar, Germany) and thaw mounted onto indium-tin-oxide coated conductive slides (Bruker Daltonik, Bremen, Germany). For cell metabolite imaging, the sections were coated with 9-aminoacridine hydrochloride monohydrate matrix (Sigma-Aldrich, Germany) at 10 mg/ml in

water/methanol 30:70 (v/v) by a SunCollect™ automatic sprayer (Sunchrom, Friedrichsdorf, Germany). Fine droplets of matrix were deposited onto the tissue section at variable flow rates over 8 layers. The first three layers were performed at 10  $\mu$ l/min, 20  $\mu$ l/min and 30  $\mu$ l/min, respectively. The last five layers were set at 40  $\mu$ l/min. MALDI-MSI was performed using a Bruker Solarix 7T FTICR-MS (Bruker Daltonik, Bremen, Germany) in negative ion mode with a lateral resolution of 50  $\mu$ m. Ions were detected over a mass range of  $m/z$  50 to 1000 using 50 laser shots at a frequency of 500 Hz.

Raw data are provided under <http://dx.doi.org/10.15134/2017M0001>.

#### **MALDI-TOF: Protein and Hormone Imaging**

Frozen tissues sections were briefly fixed in 70% ethanol and 100% ethanol for one minute each, air-dried, subsequently coated with matrix (10 g/L sinapinic acid, 60% acetonitrile, 0.2% trifluoroacetic acid) using an ImagePrep spray device (Bruker Daltonik GmbH, Bremen, Germany) using the standard protocol. MALDI-TOF measurements were carried out on an Ultraflex III MALDI tandem time-of flight (MALDI-TOF/TOF) mass spectrometer equipped with a Smartbeam laser (Bruker Daltonik GmbH). The parameters of MALDI-TOF measurements were as follows: spatial resolution of 50  $\mu$ m in positive linear mode; mass-to-charge ratio ( $m/z$ ) range, 2000–23000; sampling rate 0.1 GS/s. For each position measured, a total of 200 laser shots were accumulated. For data analysis, the software packages FlexImaging 4.0, ClinProTools and FlexControl 3.0 (Bruker Daltonik GmbH) were used.

After MALDI imaging measurement, matrix was removed with 70% ethanol, sections were stained with Hematoxylin and Eosin. The tissue slides were scanned at 20x objective magnification using a digital slide scanner (Mirax Desk, Carl Zeiss MicroImaging GmbH, Jena, Germany). Images were imported into the FlexImaging 4.0 software (Bruker Daltonik GmbH) and co-registered with MALDI imaging data.

#### **Annotation of Molecules**

Metabolites were annotated by matching the accurate mass spectrometric  $m/z$  values to database (mass accuracy  $\leq 7$  ppm, METLIN, <http://metlin.scripps.edu/>) and using the software SmartFormula (Bruker Daltonik GmbH, Bremen, Germany) or by comparing on-tissue MS/MS spectra with those of standard compounds that have been published previously (Buck et al., 2015; Sun et al., 2014, 2016). For metabolic pathway analyses we used the annotated molecules that were also annotated in KEGG (<http://www.kegg.jp>). Proteins and hormones were annotated according to our previously published and publically available database MaTisse (Maier et al., 2013).

#### **Insulin Secretion**

Cells were seeded into 96-well plates at a density of 25,000 cells/well in DMEM containing 25 mM glucose. After 3 days, the standard culture medium was replaced with fresh medium containing 5 mM glucose for 16 hr. The cells were subsequently washed twice with KRH bicarbonate buffer containing 2 mM glucose and starved in the same buffer for 2 hr. Later, starvation medium was aspirated, and cells were incubated in KRH bicarbonate buffer supplemented with indicated concentrations of glucose (2mM –low glucose; 16.5mM high Glucose) and different N-acyl taurine (each 100 $\mu$ M) or acylcarnitine (10 $\mu$ M) derivatives for 2 hr. The secreted insulin was measured using the mouse ultrasensitive insulin ELISA kit (ALPCO).

#### **DNA Content**

DNA content of the cells was measured using Quant-it Picogreen dsDNA Assay Kit (Life Technologies, P7589). Min6 cells were harvested in 200 $\mu$ l RIPA buffer (150mM NaCl, 50mM Tris, 0.5% Sodium deoxycholate, 1% IGEPAL CA-630, 0.1% SDS, pH 7.4), mixed and frozen at  $-80^{\circ}\text{C}$  till the day of the measurement. After thawing, the samples were centrifuged for 10min at 4000 g/  $10^{\circ}\text{C}$ . The supernatant was diluted 1:4 in 1xTE buffer (10 mM Tris-HCl, 1 mM EDTA, pH 7.5). Afterward, 100 $\mu$ l of each sample/standard were transferred to a black 96-Well plate and the reaction was started by adding 100 $\mu$ l Picogreen Mix (diluted 1:100 in 1xTE). After 2–5 min, samples were excited at 480 nm and the fluorescence emission intensity was measured at 520 nm on a fluorescence microplate reader (PHERAstar, BMG). The DNA concentration of the samples was calculated using the fluorescence emission intensity plotted versus DNA concentration of the standard curve.

#### **Cellular Bioenergetics**

A Seahorse extracellular flux analyzer XF24 (Agilent Technology) was used to determine oxygen consumption rate (OCR). Cells were seeded into XF24-well plates at a density of 40,000 cells/well in DMEM containing 25 mM glucose. After 3 days, the standard culture medium was replaced with fresh medium containing 5 mM glucose for 16 hr. On day 4 the cells were washed twice with bicarbonate-free KRH buffer containing 2 mM glucose and starved in the same buffer (ctrl) or plus 100 $\mu$ M acetylcarnitine or 100 $\mu$ M stearyl carnitine for 2h in a non- $\text{CO}_2$  incubator. After recording basal cellular respiration, cells were treated sequentially with glucose (16.5 mM), oligomycin (2  $\mu$ g/ml), and rotenone/antimycin A (1 and 2  $\mu$ M, respectively) to correct for non-mitochondrial respiration.

#### **Electron Microscopy**

Tissues and cells were fixed in 2.5% electron microscopy grade glutaraldehyde in 0.1 M sodium cacodylate buffer pH 7.4 (Science Services, Munich, Germany), postfixed in 2% aqueous osmium tetroxide (Dalton, 1952), dehydrated in gradual ethanol (30%–100%) and propylene oxide, embedded in Epon (Merck, Darmstadt, Germany) and cured for 24 hr at  $60^{\circ}\text{C}$ . Semithin sections were cut and stained with toluidine blue. Ultrathin sections of 50 nm were collected onto 200 mesh copper grids, stained with uranyl acetate and lead citrate before examination by transmission electron microscopy (Zeiss Libra 120 Plus, Carl Zeiss NTS GmbH,

Oberkochen, Germany). Pictures were acquired using a Slow Scan CCD-camera and ITEM software (Olympus Soft Imaging Solutions, Münster, Germany).

### Immunofluorescence, Immunohistochemistry, and Image Analysis

Tissues were formalin-fixed and paraffin embedded. For immunofluorescence staining, tissues were sliced in 4  $\mu$ m thick sections and mounted onto poly-L-lysine-coated glass slides. Pancreatic islet were analyzed by a triple staining for insulin (polyclonal guinea pig anti-insulin, A0564, Dako, USA; biotinylated goat anti-guinea pig IgG, BA-7000, Vector Laboratories, USA; streptavidin – FITC, 434311, Thermo Fisher Scientific, USA), glucagon (polyclonal rabbit anti-glucagon, ab8055, Abcam, UK; Cy3 - goat anti-rabbit, A10520, Thermo Fisher Scientific, USA) and PDX1 (polyclonal goat anti-PDX1, ab47383, Abcam, UK; Alexa Fluor 660 - donkey anti-Goat IgG). Nuclei were identified with Hoechst 33342. Fluorescence stainings were photographed with an Axio Imager Z1 (Zeiss) and visualized with the Axio Vision 4.6.3 software (Zeiss).

Microscopic images were evaluated using the commercially available image analysis software Definiens Developer XD2 (Definiens AG, Germany) by detecting the specific stained tissue area of glucagon, insulin, PDX and DAPI. The regions of interest, e.g., Langerhans islets, were annotated manually and finally the ratio of glucagon, insulin, PDX area respectively to DAPI area was calculated.

For immunohistochemical staining, tissues were sliced in 4  $\mu$ m thick sections and mounted onto poly-L-lysine-coated glass slides. Immunohistochemical staining was performed on a Discovery XT automated stainer (Ventana, Tucson, AZ, USA). As primary antibodies rabbit anti-CPT1a (Acris Antibodies, Herford, Germany) at a dilution of 1:50, rabbit anti-CPT2 (Abcam, Cambridge, United Kingdom) at a dilution of 1:50, rabbit anti- fatty acid amide hydrolase (Abcam, Cambridge, United Kingdom) at a dilution of 1:500 were used. Secondary antibody was goat anti-rabbit (Vector Laboratories, Peterborough, United Kingdom) at a dilution of 1:750. Signal detection was performed using peroxidase-DAB (diaminobenzidine)-MAP chemistry (Roche, Ventana, Tucson, AZ, USA).

All stained slides were scanned at 20x objective magnification using a Mirax Desk digital slide scanner (Carl Zeiss MicroImaging, Munich, Germany), and the resulting images were imported into image analysis software.

Images obtained by CPT1a, CPT2 and FAAH staining were analyzed using the commercially available image analysis software Definiens TissueStudio3 (Definiens AG; München, Germany). The regions of interest, the LHs, were manually annotated and a specific rule set was defined to detect the cytoplasm within each defined region. The quantified parameter was mean brown intensity of the cytoplasm within each defined region, calculated as a relative unit.

## QUANTIFICATION AND STATISTICAL ANALYSIS

### Bioinformatics, Statistical Analysis

MATLAB R2013a (v.7.10.0, MathWorks, Natick, MA) was used as MALDI spectral pre-processing tool for the subsequent bioinformatics data analysis according to previous publications (Buck et al., 2015; Sun et al., 2016). Briefly, the exported spectra of defined regions of interest underwent a self-implemented MATLAB analysis pipeline that was generated based on the work of McDonnell et al. 2010 (McDonnell et al., 2010). Baseline correction was done by interpolating between given equally spaced intervals (spacing 0.02 Da). Resampling was performed using a 0.005 Da step width, and the smoothing operation was carried out using a Kaiser-Window of size 3. Using an adapted version of the LIMPIC algorithm (Mantini et al., 2007), peaks were picked using a minimal peak width of 0.0005, a noise-threshold of 4 and an intensity threshold percentage of 0.01. Peaks were generated if found in 80% of the samples in each group. Clear isotopes were excluded.

To identify statistically significant differences in  $m/z$  values, the peaks were analyzed with the Mann-Whitney  $U$  test and corrected in context of multiple comparisons using the Benjamini-Hochberg correction ( $\alpha = 0.05$ ).  $p \leq 0.05$  was considered statistically significant ( $p \leq 0.05 = *$ ,  $p \leq 0.01 = **$ ,  $p \leq 0.001 = ***$ ).

Correlation evaluations were performed by Pearson correlation. Again,  $p \leq 0.05$  was considered statistically significant.

### Network Generation

Metabolic networks were generated for each disease state, prediabetes and diabetes. To this end, peaks were first reduced to those peaks that overlapped between the two mouse lines for the respective state. Gaussian graphical models (GGMs), which are based on partial correlation coefficients, were then calculated using the 'GeneNet' R package. Previous studies have shown that GGMs reconstruct true metabolic networks from metabolomics data (Krumsek et al., 2011, 2012; Shin et al., 2014). An edge (link, line) was drawn between two metabolites if their pairwise partial correlation was significant at a false discovery rate (FDR) of 0.01.

**Supplemental Information**

**N-acyl Taurines and Acylcarnitines Cause  
an Imbalance in Insulin Synthesis and Secretion  
Provoking  $\beta$  Cell Dysfunction in Type 2 Diabetes**

**Michaela Aichler, Daniela Borgmann, Jan Krumsiek, Achim Buck, Patrick E. MacDonald, Jocelyn E. Manning Fox, James Lyon, Peter E. Light, Susanne Keipert, Martin Jastroch, Annette Feuchtinger, Nikola S. Mueller, Na Sun, Andrew Palmer, Theodore Alexandrov, Martin Hrabe de Angelis, Susanne Neschen, Matthias H. Tschöp, and Axel Walch**

## **Supplemental Information**

### **N-acyl Taurines and Acylcarnitines Cause an Imbalance in Insulin Synthesis and Secretion Provoking $\beta$ -Cell Dysfunction in Type 2 Diabetes**

#### **Authors**

**Michaela Aichler, Daniela Borgmann, Jan Krumsiek, Achim Buck, Patrick E. MacDonald, Jocelyn E. Manning Fox, James Lyon, Peter E. Light, Susanne Keipert, Martin Jastroch, Annette Feuchtinger, Nikola S. Mueller, Na Sun, Andrew Palmer, Theodore Alexandrov, Martin Hrabe de Angelis, Susanne Neschen, Matthias H. Tschöp, Axel Walch**

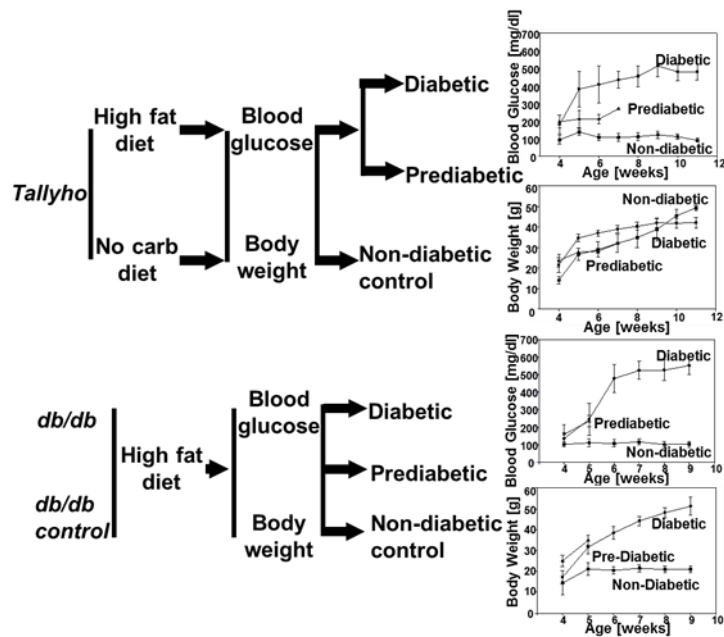


**Figure S1. Experimental setup of study groups, Related to STAR Methods, Figure 1 and Figure 2.**

We used two different diabetes mouse models to determine the metabolic alterations of  $\beta$ -cells during the progression of T2D that are not specifically representative of a particular genetic background. The BKS.Cg-Cock7m+/+Leprdb/J (*db/db*) mouse represents a common model widely used for antidiabetes drug testing, however it develops monogenic obesity due to disruption of leptin-receptor signaling. In contrast *TallyHo/JngJ* (*TallyHo*) mice recapitulate broader aspects of polygenic human “diabesity”. Based on their phenotypic parameters, animals were included that either presented a prediabetic or overtly diabetic disease state in addition to non-diabetic controls.

## Immunofluorescence

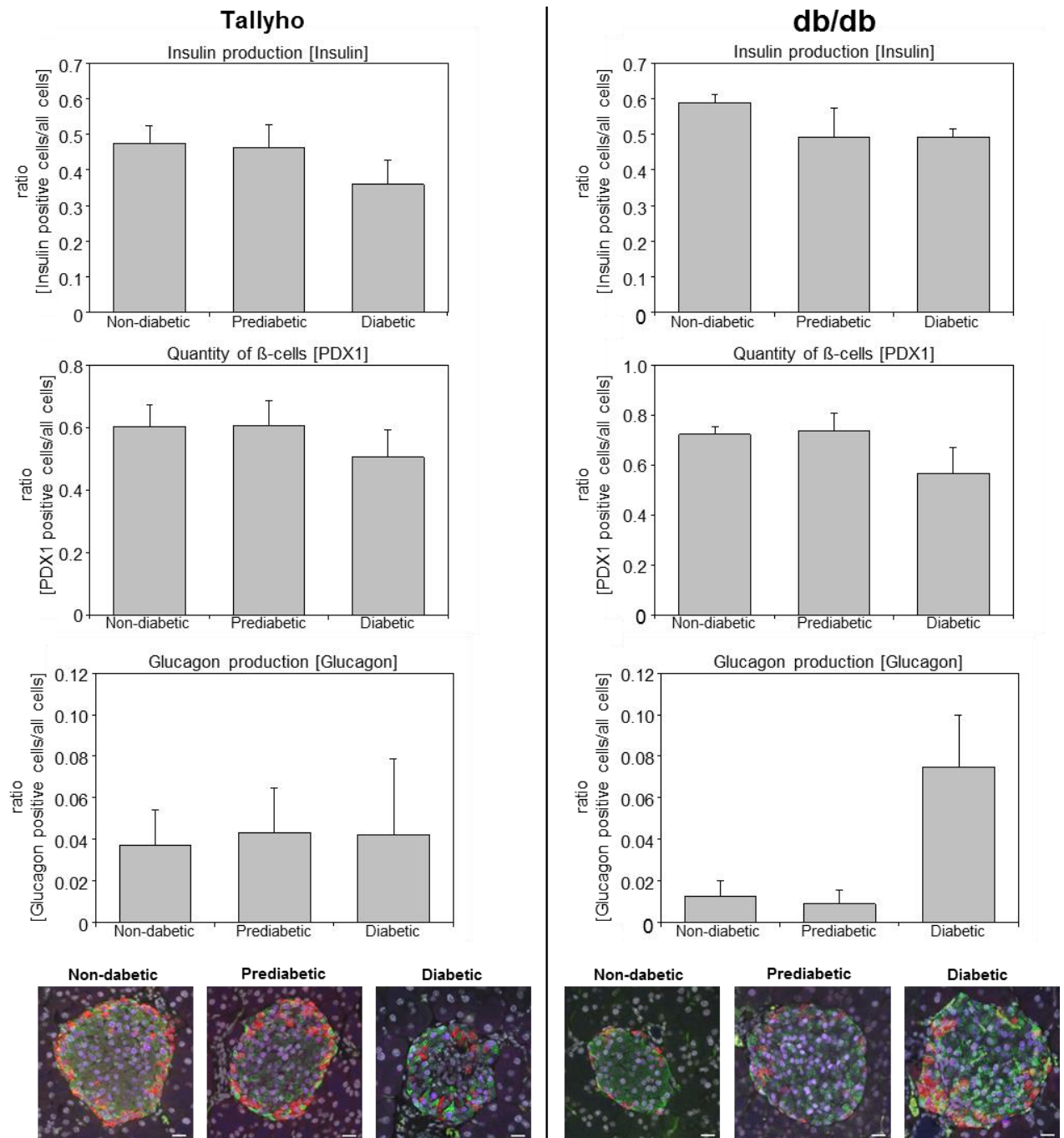
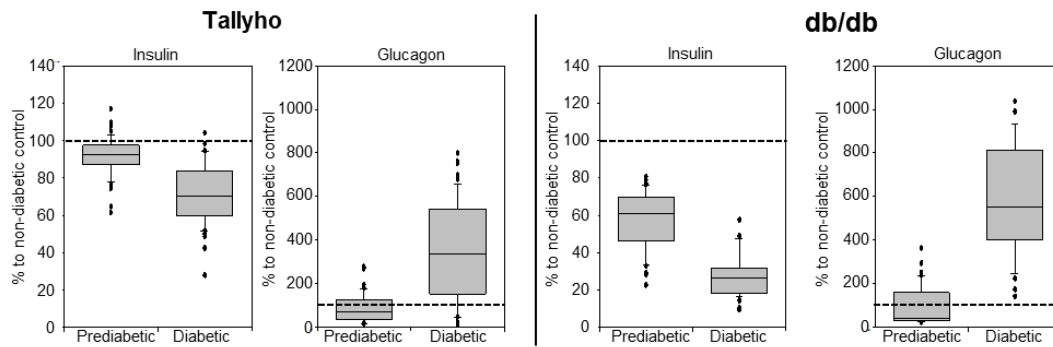


**Figure S2. Determination of overall quality and composition of LHI by immunofluorescence, Related to Figure 1.**

Quantitative analysis of immunofluorescence for insulin, PDX1 and glucagon. Insulin production was reduced as the disease progressed. The quantity of  $\beta$ -cells was comparable between prediabetic mice and non-diabetic controls and was only slightly, but not significantly, reduced in overtly diabetic mice. Glucagon production changed as expected with progression of the disease. Data are represented as the mean  $\pm$  SEM. Examples of immunofluorescence stained LHI are presented (green: insulin, red: glucagon, blue: PDX1, grey: DAPI; scale bar 20  $\mu$ m). Data are presented as mean  $\pm$  SEM.

## **A** MALDI-Hormone Imaging – mouse Langerhans Islets in intact immediated environment



## **B** MALDI-Hormone Imaging – isolated human Langerhans islets

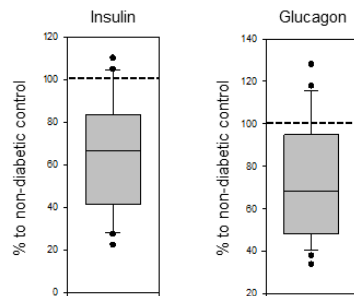


**Figure S3. Determination of the overall quality and composition of LHI by MALDI-Hormone imaging, Related to Figure 1 and Figure 2.**

(A) MALDI-TOF analyses of insulin and glucagon contents confirmed the results for LHI from mice. (B) The insulin and glucagon contents of isolated human LHI were both reduced in patients with T2D compared with healthy controls.

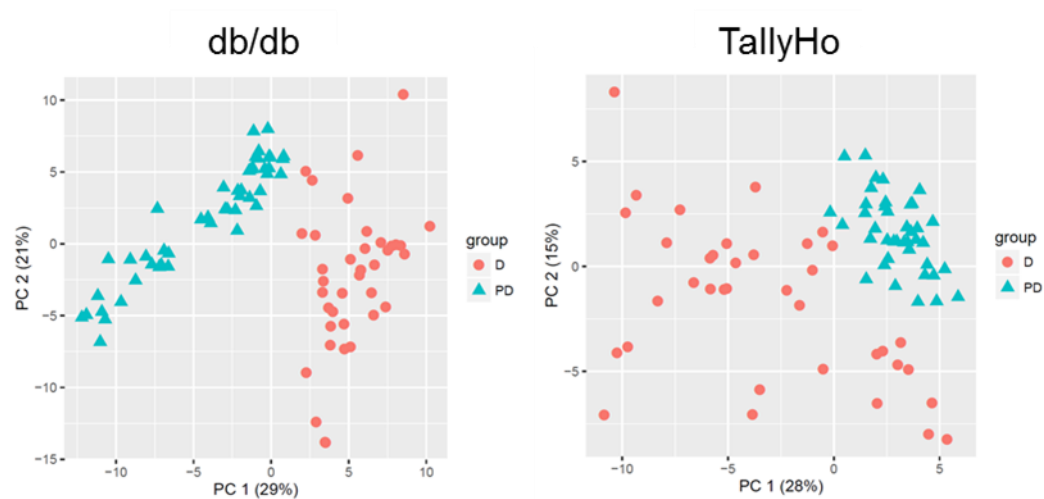


**Figure S4. Clear molecular separation between the disease states in mice, Related to Figure 2.**

Principal component analysis of the molecular individuality of the prediabetic and overtly diabetic groups in each mouse model revealed a clear molecular separation between the disease states.

# Genetic Correlation Network

6

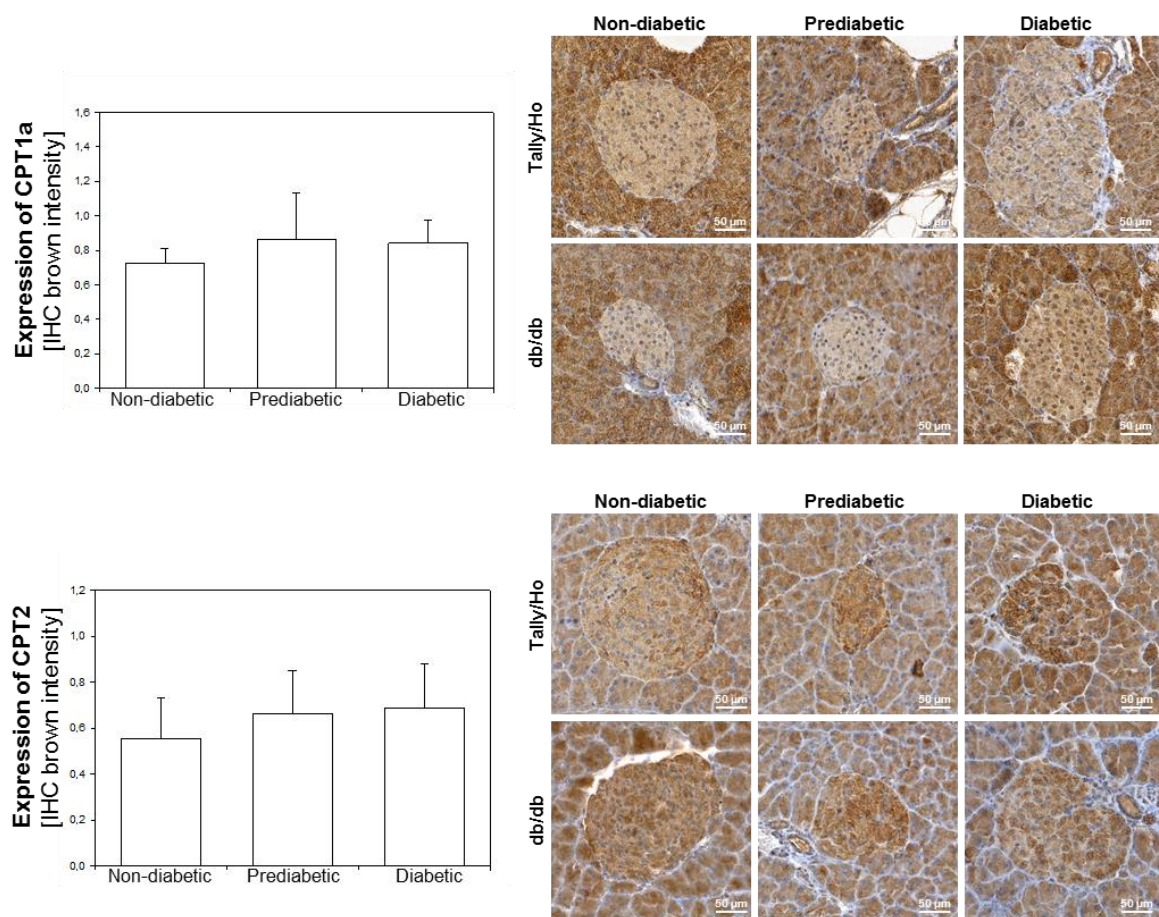


**Figure S6. Expression of CPT1a and CPT2 in Langerhans islets, Related to Figure 5.**

There was no significant difference in the expression of CPT1a or CPT2 between non-diabetic, prediabetic, and diabetic groups.

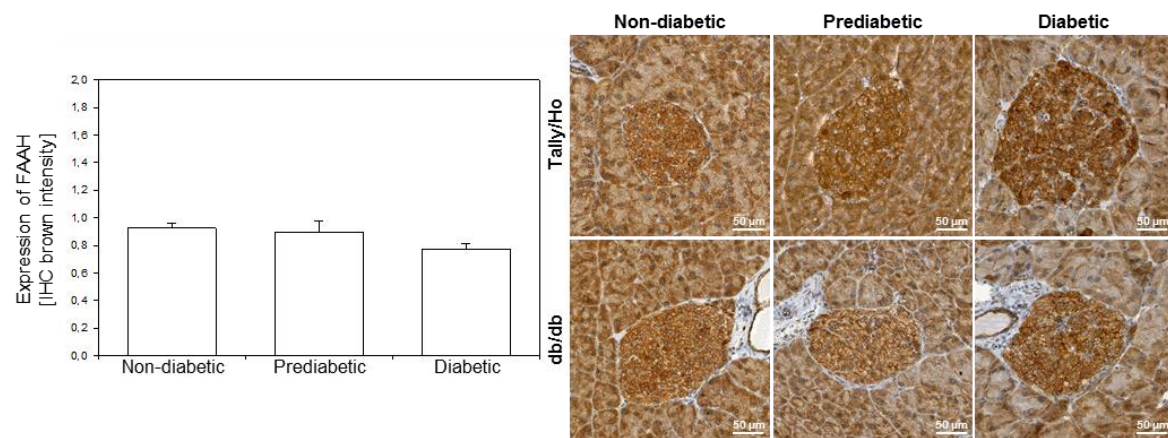


**Figure S7. Expression of FAAH, Related to Figure 7.**

The expression of FAAH was not significantly different between non-diabetic, prediabetic, and diabetic groups.

**A**

	Tallyho			db/db		
	Prediabetic	Diabetic	Contr.	Prediabetic	Diabetic	Contr.
Mice [n=x]	4	6	4	5	5	5
Body weight [g]	29.1 $\pm$ 0.7	41.0 $\pm$ 0.7	37.8 $\pm$ 2.4	34.9 $\pm$ 0.9	48.9 $\pm$ 1.2	22.7 $\pm$ 0.6
Blood glucose [mg/dl]	237.7 $\pm$ 15.8	504.1 $\pm$ 17.8	110.2 $\pm$ 6.0	233.3 $\pm$ 12.3	542.3 $\pm$ 19.2	107.4 $\pm$ 6.2

**B**

	Tallyho			db/db		
	Prediabetic	Diabetic	Contr.	Prediabetic	Diabetic	Contr.
Langerhans Islets [n=x]	40	37	66	49	39	32
Differential masses vs. Control [n=x]	495	653		785	651	

**Table S1. Overview of experimental groups, physiological parameters and detected metabolites, Related to STAR Methods, Figure S1 and Figure 2.**

(A) Study groups and physiological parameters. (B) 263 LHIs were analyzed for in situ-metabolomics.

A

## Annotated molecules correlating with blood glucose

### Prediabetic condition

annotated molecule	Succinate	Pyrophosphate	Leucine/Isoleucine	Cytidine	Deoxy-ribose-phosphate	Palmitic acid
accuracy [ppm]	0	1	1	7	1	0
ion	[M+Cl]-	[M-H <sub>2</sub> O-H]-	[M+K-2H]-	[M-H <sub>2</sub> O-H]-	[M+K-2H]-	[M-H]-
m/z	152.996	158.925	168.043	224.069	250.9725	255.233
Correlation Coefficient	-0.339	-0.33	0.293	0.321	-0.298	0.399
P Value	0.00652	0.00826	0.0197	0.0103	0.0175	0.0012
annotated molecule	Oleic acid	Stearic acid	AMP/cAMP	GMP	UDP	Palmitoyl-carnitine
accuracy [ppm]	2	0	0	1	0	0
ion	[M-H]-	[M-H]-	[M-H]-	[M+K-2H]-	[M+Na-2H]-	[M+K-2H]-
m/z	281.248	283.264	328.045	400.006	424.9767	436.2835
Correlation Coefficient	0.476	0.434	-0.331	0.324	-0.357	0.503
P Value	0.0000815	0.000386	0.00798	0.00954	0.00409	0.0000309
annotated molecule	ADP	Linoleyl carnitine/ Linoelaidyl carnitine	Stearyl carnitine	ATP		
accuracy [ppm]	0		2	0		
ion	[M+Na-2H]-	[M+K-2H]-	[M+K-2H]-	[M-H]-		
m/z	448.004	460.283	464.3137	505.9885		
Correlation Coefficient	-0.53	0.391	0.397	-0.321		
P Value	0.0000805	0.00183	0.00186	0.0111		

**Table S2B**

### Diabetic condition

annotated molecule	Pyrophosphate	Cytidine	N-Acetyl-glucosamine phosphate	N-Acetyl-glucosamine phosphate	AMP/cAMP	N-Acetylmuramic acid phosphate
accuracy [ppm]	4	1	2	1	3	6
ion	[M-H <sub>2</sub> O-H]-	[M-H]-	[M-H <sub>2</sub> O-H]-	[M-H]-	[M-H]-	[M-H]-
m/z	158.9255	242.0785	282.0385	300.0495	328.0465	372.0725
Correlation Coefficient	-0.57	0.663	-0.456	-0.469	-0.59	-0.564
P Value	0.00102	0.000563	0.0114	0.00888	0.000606	0.00116
annotated molecule	UDP					
accuracy [ppm]	2					
ion	[M-H]-					
m/z	402.996					
Correlation Coefficient	-0.444					
P Value	0.0139					

**Table S2: Correlation of metabolites with blood glucose, Related to Figure 2.** (A) Correlation of annotated metabolites with blood glucose in prediabetes. (B) Correlation of annotated metabolites with blood glucose in diabetes.

A

## Annotated molecules correlating with insulin content

### Prediabetic condition

annotated molecule	Pyrophosphate	Leucine/Isoleucine	Pyrophosphate	N2-Acetyl-L-ornithine	Cytidine	Acetylcarnitine
accuracy [ppm]	1	1	0	7	7	3
ion	[M-H <sub>2</sub> O-H]-	[M+K-2H]-	[M-H]-	[M+Cl]-	[M-H <sub>2</sub> O-H]-	[M+K-2H]-
m/z	158.925	168.043	176.936	209.0715	224.069	240.0635
Correlation Coefficient	0.277	-0.435	0.357	0.26	-0.35	0.66
P Value	0.0278	0.000369	0.00412	0.0448	0.00486	5.67E-08
annotated molecule	Deoxy-ribose-phosphate	Palmitic acid	N-Acetyl glucosamine	PPPi	Phospho-gluconic acid	N-Ornithyl-L- taurine
accuracy [ppm]	1	0	3	0	0	7
ion	[M+K-2H]-	[M-H]-	[M+Cl]-	[M-H]-	[M-H <sub>2</sub> O-H]-	[M+Na-2H]-
m/z	250.9725	255.233	256.0585	256.9025	257.0065	260.0705
Correlation Coefficient	0.428	-0.311	0.697	0.474	0.457	-0.288
P Value	0.00047	0.0131	8.61E-10	0.000114	0.000166	0.0219
annotated molecule	Oleic acid	N-Acetyl glucosamine phosphate	Stearic acid	CMP	AMP/cAMP	GMP
accuracy [ppm]	2	2	0	1	0	0
ion	[M-H]-	[M-H <sub>2</sub> O-H]-	[M-H]-	[M-H]-	[M-H]-	[M-H]-
m/z	281.248	282.0385	283.264	322.044	328.045	362.0505
Correlation Coefficient	-0.305	0.288	-0.325	-0.486	0.259	-0.745
P Value	0.015	0.0221	0.00934	0.0000537	0.0404	2.53E-12
annotated molecule	N-Acetylmuramic acid 6-phosphate	UDP	N-linoleoyl taurine	N-oleoyl taurine	N-stearoyl taurine	GMP
accuracy [ppm]	0	0	0	0	1	1
ion	[M-H]-	[M-H <sub>2</sub> O-H]-	[M-H]-	[M-H]-	[M-H]-	[M+K-2H]-
m/z	372.07	384.9835	386.237	388.2525	390.2677	400.006
Correlation Coefficient	-0.466	0.25	-0.607	-0.453	-0.532	-0.423
P Value	0.000151	0.0483	1.31E-07	0.000191	0.00000709	0.000548
annotated molecule	ADP	Stearyl carnitine	ATP	UDP-glucose/ galactose		
accuracy [ppm]	0	2	0	2		
ion	[M+Na-2H]-	[M+K-2H]-	[M-H]-	[M-H]-		
m/z	448.004	464.3137	505.9885	565.0465		
Correlation Coefficient	0.262	-0.386	0.309	-0.618		
P Value	0.0381	0.00252	0.0144	1.82E-07		

**Table S3: Correlation of metabolites with insulin content. Related to Figure 2, 3, 4, 5, 6, 7.**

(A) Correlation of annotated metabolites with insulin in prediabetes.

## B

### Annotated molecules correlating with insulin content

#### Diabetic condition

annotated molecule	Pyrophosphate	Deoxyribose phosphate	Cytidine	Glucose-phosphate	N-Acetyl glucosamine phosphate	Eicosadienoic acid
accuracy [ppm]	4	0	1	2	2	2
ion	[M-H <sub>2</sub> O-H]-	[M-H]-	[M-H]-	[M-H]-	[M-H <sub>2</sub> O-H]-	[M-H]-
m/z	158.9255	213.017	242.0785	259.023	282.0385	307.265
Correlation Coefficient	0.487	0.397	-0.439	0.429	0.487	0.555
P Value	0.00636	0.0404	0.0362	0.0179	0.00641	0.00176
annotated molecule	AMP/cAMP	N-Acetylmuramic acid 6-phosphate	UDP			
accuracy [ppm]	3	6	2			
ion	[M-H]-	[M-H]-	[M-H]-			
m/z	328.0465	372.0725	402.996			
Correlation Coefficient	0.422	0.457	0.43			
P Value	0.0201	0.0111	0.0176			

**Table S3: Correlation of metabolites with insulin content. Related to Figure 2, 3, 4, 5, 6, 7.**

(B) Correlation of annotated metabolites with insulin in diabetes.